

AGU Advances

RESEARCH ARTICLE

10.1029/2024AV001264

Peer Review The peer review history for this article is available as a PDF in the Supporting Information.

Key Points:

- Topographic roughness at scales of meters to tens of meters reflects a balance between roughening and smoothing processes
- Analytical expressions for topographic roughness exist for many settings
- Increasingly high-resolution topographic data is a valuable resource for extracting process-specific information from topographic roughness

Supporting Information:

Supporting Information may be found in the online version of this article.

Correspondence to:

T. H. Doane,
doanet@iu.edu

Citation:

Doane, T. H., Gearon, J. H., Martin, H. K., Yanites, B. J., & Edmonds, D. A. (2024). Topographic roughness as an emergent property of geomorphic processes and events. *AGU Advances*, 5, e2024AV001264. <https://doi.org/10.1029/2024AV001264>

Received 1 APR 2024

Accepted 18 AUG 2024

Author Contributions:

Conceptualization: T. H. Doane, J. H. Gearon, H. K. Martin, B. J. Yanites, D. A. Edmonds

Formal analysis: T. H. Doane

Writing – original draft: T. H. Doane, J. H. Gearon, H. K. Martin, B. J. Yanites, D. A. Edmonds

Writing – review & editing: T. H. Doane, J. H. Gearon, H. K. Martin, B. J. Yanites, D. A. Edmonds

© 2024. The Author(s).

This is an open access article under the terms of the [Creative Commons](#)

[Attribution License](#), which permits use, distribution and reproduction in any medium, provided the original work is properly cited.

Topographic Roughness as an Emergent Property of Geomorphic Processes and Events



T. H. Doane^{1,2,3} , J. H. Gearon² , H. K. Martin^{2,4,5} , B. J. Yanites² , and D. A. Edmonds² 

¹Division of Hydrologic Sciences, Desert Research Institute, Las Vegas, NV, USA, ²Earth and Atmospheric Sciences, Indiana University Bloomington, Bloomington, IN, USA, ³Earth, Environmental, and Planetary Sciences, Case Western Reserve University, Cleveland, OH, USA, ⁴Geological and Planetary Sciences, California Institute of Technology, Pasadena, CA, USA, ⁵Resnick Sustainability Institute, California Institute of Technology, Pasadena, CA, USA

Abstract Earth's terrestrial surfaces commonly exhibit topographic roughness at the scale of meters to tens of meters. In soil- and sediment-mantled settings topographic roughness may be framed as a competition between roughening and smoothing processes. In many cases, roughening processes may be specific eco-hydro-geomorphic events like shrub deaths, tree uprooting, river avulsions, or impact craters. The smoothing processes are all geomorphic processes that operate at smaller scales and tend to drive a diffusive evolution of the surface. In this article, we present a generalized theory that explains topographic roughness as an emergent property of geomorphic systems (semi-arid plains, forests, alluvial fans, heavily bombarded surfaces) that are periodically shocked by an addition of roughness which subsequently decays due to the action of all small scale, creep-like processes. We demonstrate theory for the examples listed above, but also illustrate that there is a continuum of topographic forms that the roughening process may take on so that the theory is broadly applicable. Furthermore, we demonstrate how our theory applies to any geomorphic feature that can be described as a pit or mound, pit-mound couplet, or mound-pit-mound complex.

Plain Language Summary Earth's surface is constantly roughened by processes that operate quasi-randomly in space and time. For example, in forest settings, trees that topple will uproot soil and deposit a mound and excavate a pit, leaving a pit-mound couplet on the surface. With time, this topographic signature decays due to geomorphic processes rearranging sediment and soil on the surface. In this paper, we develop theory that explains topographic roughness as a balance between processes that create roughness and those that destroy it. We consider several different mechanisms (desert shrub mounds, tree uprooting, river channel avulsions, and impact cratering) and develop a general theory for topographic roughness that applies to many settings. We further develop theory that allows for a very wide range of natural features that may not be well-described by simple geometric functions.

1. Introduction

A central goal of geomorphology is to clarify the relationships between surface processes and ecology (Furbish et al., 2009; Gabet et al., 2003; Gabet & Mudd, 2010), climate (Madoff & Putkonen, 2016, 2022; Richardson et al., 2019), solid earth processes (Booth et al., 2017; Finnegan et al., 2021; LaHusen et al., 2016; Richardson & Karlstrom, 2019; Roering et al., 2015), and weather (DeLisle & Yanites, 2023; Doane et al., 2023; Turowski et al., 2009). An obstacle to progress toward that goal is that the relevant spatial and temporal scales of surface processes often differ from those of human observation, frustrating scientific progress. Instead of direct observation and measurement of processes, there is a legacy in geomorphology that relies on the connection between process and topographic form which allows for process information to be extracted from topographic morphometrics (Clubb et al., 2016; Fernandes & Dietrich, 1997; Gabet et al., 2021; Grieve et al., 2016; Roering et al., 2007; Struble & Roering, 2021). Until recent decades, most topographic data sets had spatial or horizontal resolutions of 10–30 m, and many theoretical, field-based, and modeling efforts, purposefully or not, targeted that scale. This led to an understanding of processes at that scale or larger (Ganti et al., 2012) but implicitly obscured smaller scale processes. In recent decades, there has been tremendous technological development and a significant increase in the coverage, precision, and resolution of topographic data sets (Lewis et al., 2020; Luetzenburg et al., 2021; Stoker & Miller, 2022; Viles, 2016). High resolution topographic data sets (i.e., <2 m horizontal resolution) allow us to target increasingly precise processes like tree throw (Doane et al., 2021, 2023), as opposed to the suite of processes that determine large scale morphometrics (Figure 1). Despite increasingly high-resolution

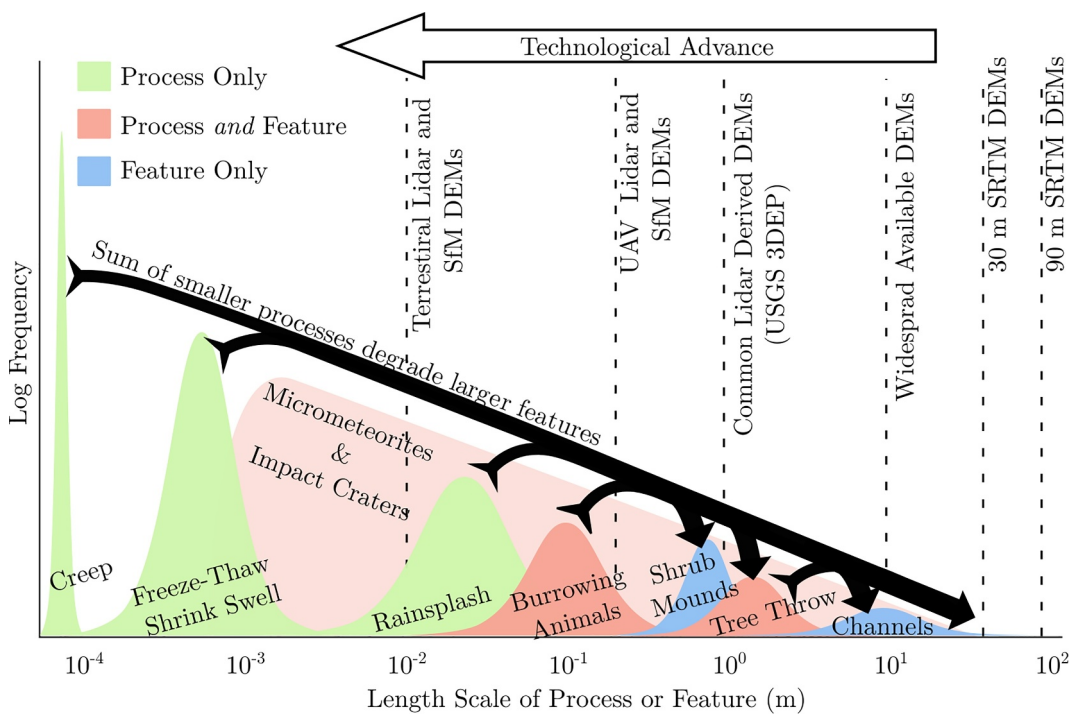


Figure 1. Conceptual plot of the frequency and length scale of processes and features. For any given landscape, the frequency of certain processes may increase or decrease so that this plot will be unique for a given setting.

topographic data, the legacy of coarse-scale geomorphology persists as researchers apply low-pass filters to high-resolution topographic data to address long timescale issues such as erosion rates measured over 10 ka, which justifies the spatial averaging (Ganti et al., 2012), but removes small scale, detailed topographic features from analyses. This article provides a framework for extracting process-based information contained in the small wavelength topographic features that record specific eco- and hydrogeomorphic events.

At length scales larger than decimeters and smaller than tens of meters, topography is noisy and rough (DiBiase et al., 2017; Doane et al., 2021; Ganti et al., 2012; Roering et al., 2010; Roth et al., 2020). In many sediment- or soil-mantled settings, topographic roughness is stochastically created by discrete features or events. With age, those roughness elements decay due to the action of smaller scale geomorphic processes that tend to remove roughness (Furbish & Fagherazzi, 2001; Jyotsna & Haff, 1997) (Figure 1). Topographic roughness, therefore, reflects a balance between the frequency and magnitude of roughening processes and those geomorphic processes that tend to smooth the surface. We specifically refer to topographic roughness as the deviation from the average topography measured over scales of a meter to tens of meters, depending on the setting. We describe theory that presents topographic roughness as an emergent property of specific geomorphic processes. These include mounds under shrubs in semi-arid settings (Bochet et al., 2000), tree throw pit-mound couplets (Doane et al., 2021, 2023), abandoned channels on fan surfaces (Johnstone et al., 2018), and heavily cratered surfaces (Kreslavsky et al., 2013). Topographic roughness is now measurable with lidar, structure-from-motion, and lunar and planetary topographic data sets, allowing us to apply the theory to natural landscapes and invert it to learn about process rates or frequencies and statistics (Doane et al., 2023).

This paper is outlined as follows. In Section 2, we describe the general steps for developing analytical expressions for the topographic roughness (variance) of surfaces. In Section 3, we apply these steps to four different features and advocate for a view of topographic roughness as *process topography*, where we demonstrate that topographic roughness contains information about specific geomorphic processes. For some settings, we briefly discuss case studies. However, this paper primarily presents theory, and each setting warrants its own investigation. In Section 4 we generalize the theory to represent a continuum of initial conditions and explore varied autocorrelation structures of the stochastic roughening processes (shrub population dynamics, tree throw rates, avulsion

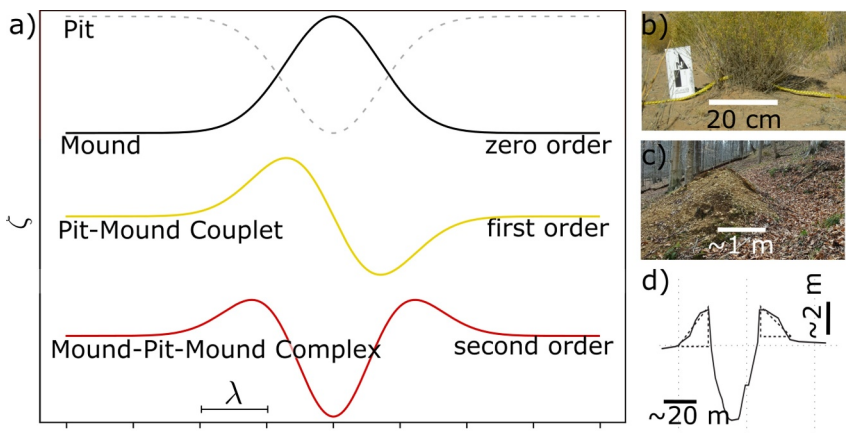


Figure 2. (a) The three basic functions which form initial conditions of roughness elements either as independent functions or as the sum of two functions. Zero (dashed line indicates a pit which is just the negative version of a mound), first, and second order DoG's roughly correspond to shrub sediment mounds (b) photo credit David Furbish) (Furbish et al., 2009), tree throw pit-mound couplets (c) (Doane et al., 2021, 2023), and channel-levee complexes (d) From Adams et al., 2004) respectively (re-published with permission from Elsevier).

frequency). In that section, we also demonstrate that topographic variance is a robust metric, and if a feature can be broadly described as a mound, pit-mound couplet, or mound-pit-mound complex (Figure 2), the theory applies.

2. Theory

2.1. Notation

We use the following notation in this paper. Hats on variables refer to the Fourier transform of the spatial variable ($\hat{\zeta}(k) \downarrow \zeta(x)$), where ζ [L] is the land-surface elevation, x [L] is a horizontal position, and k [L^{-1}] is wavenumber (radians per meter). The subscript s refers to a single feature that comprises a topographic roughness element, so r_s is the roughness due to a single feature (e.g., a mound) and r is the roughness due to the sum of features across a landscape. μ_m is the expected or mean value of variable m . Similarly, angle brackets, for example, $\langle m \rangle$, imply an average of the variable that is more convenient for certain expressions than μ -notation. The organization of this paper requires that we reuse variables and A always refers to an amplitude and λ is a length scale. A will take on subscripts ranging between 0 and 2 and have different units so that A_n has units [L^{n+1}]. H is the domain length or area and will have a subscript 1 or 2 to denote one- or two-dimensional problems. A list of variables is at the end of this paper.

2.2. Derivation

Topographic roughness is a popular yet ambiguous metric (Smith, 2014) that broadly indicates information about the variation in topography over specified measurement intervals (Kreslavsky et al., 2013). As Smith (2014) notes, the ambiguity arises from varied applications of topographic roughness, which is measured over centimeters to kilometers and is known to influence or reflect: the velocity of open channel flow over a rough bed (Hassan & Reid, 1990; Kean & Smith, 2006; Nikora et al., 2007; Yager et al., 2007), bedrock exposure on hillslopes (Milodowski et al., 2015), particle travel distances (DiBiase et al., 2017; Furbish et al., 2021; Gabet & Mendoza, 2012; Roth et al., 2020), the age of landslides (LaHusen et al., 2016), and the age of abandoned surfaces on alluvial fans (Frankel & Dolan, 2007; Johnstone et al., 2018). Popular measures of roughness include topographic variance (Doane et al., 2021, 2023; Roth et al., 2020), the root mean square of slope (Booth et al., 2017; LaHusen et al., 2016), variograms (Soulard et al., 2012), or statistics associated with the second derivative of topography (Booth et al., 2017; Kreslavski et al., 2013). Each measure is subject to the spatial scale over which it is applied, and each measure may be better suited for a different purpose (Kreslavski et al., 2013 provide a good summary of consequences of roughness metrics). We use the topographic variance definition because it is the most mathematically accessible to analytical solutions. There are several relevant spatial scales for the settings in this article. The topographic variance for shrub mounds is measured over meters to tens of meters; for pit-mound

couplets, it is measured over tens to hundreds of meters; for alluvial fans, it is measured over hundreds to thousands of meters; and for cratered surfaces from tens of meters, to tens of kilometers.

Topographic roughness (quantified by topographic variance) in soil- or sediment-mantled settings has a simple interpretation: it reflects a balance between a stochastic roughening process and the suite of slope-dependent processes that chronically degrade topography (Doane et al., 2021; Furbish & Fagherazzi, 2001; Jyotsna & Haff, 1997; Schumer et al., 2017). This sets up a simple mathematical statement. We anticipate that the expected (or average) topographic roughness, μ_r [L^2], scales linearly with the ratio of roughness production rate, μ_p [T^{-1}], to the magnitude of creep-like processes as represented by a topographic diffusivity, K [$L^2 T^{-1}$] so that

$$\mu_r = C \frac{\mu_p}{K} \quad (1)$$

where C is a coefficient that depends on the geometry of the feature (mound, pit-mound couplet, mound-pit-mound complex), and as a reminder, μ_p and μ_r are mean roughening rates and roughness values respectively. Equation 1, which can be inverted for a production rate, highlights the potential for using topographic roughness to interpret process rates or frequencies that are otherwise difficult to observe (Doane et al., 2021). For example, tree throw is rarely directly observed and obtaining frequencies typically depends on measuring the impact of specific storms and multiplying that effect by the storm frequency (Hancock & Lowry, 2021; Hellmer et al., 2015). However, in Doane et al. (2023), the authors point out that these extreme events have long return intervals, such that direct observations are usually not possible. Topographic roughness, on the other hand, is formed by individual storms and persists for many decades to centuries and is thus a useful archive of tree throw.

Chronic small-scale geomorphic processes tend to drive bulk downslope transport at rates that scale with the land-surface slope. This leads to a model of land surface evolution that takes the form of a linear diffusion equation (Culling, 1963; Fernandes & Dietrich, 1997),

$$\frac{\partial \zeta}{\partial t} = K \nabla^2 \zeta, \quad (2)$$

where ζ [L] is the land surface elevation, K [$L^2 T^{-1}$] is the topographic diffusivity that reflects the magnitude of small-scale creep-like processes, and t [T] is time. The diffusion equation smooths topography at a rate that depends on the form of the roughness feature and the magnitude of K (Doane et al., 2021; Furbish & Fagherazzi, 2001; Jyotsna & Haff, 1997). We note that nonlinear (Roering et al., 1999) and nonlocal (Foufoula-Georgiou et al., 2010; Furbish & Haff, 2010; Tucker & Bradley, 2010) formulations for sediment transport and land surface evolution are alternative models. While such models may perform better in certain settings in recreating ridge and valley scale morphology, we argue that for the small-scale processes that we consider here, linear diffusion captures the essence of the process and is a reasonable description. Furthermore, nonlinear and nonlocal formulations preclude analytical solutions for topographic roughness, but one could conduct a similar study numerically. The problems in this paper have analytical or quasi-analytical solutions to the diffusion equation achieved in the wavenumber domain via the Fourier transform. The wavenumber representation of an analytical solution to (Equation 2) is

$$\hat{\zeta}(t, k_x, k_y) = \hat{\zeta}(0, k_x, k_y) e^{-Kt(k_x^2 + k_y^2)}, \quad (3)$$

where k_x and k_y are wavenumbers [L^{-1}] (radians per distance). We then take advantage of Parseval's Theorem which states that the integral of the square of the Fourier transform of a signal is equal to the integral of the square of the original signal,

$$\frac{1}{4\pi^2} \int_{-\infty}^{\infty} \int_{-\infty}^{\infty} |\hat{\zeta}(k_x, k_y)|^2 dk_x dk_y = \int_{-\infty}^{\infty} \int_{-\infty}^{\infty} \zeta(x)^2 dx dy. \quad (4)$$

Plugging (Equation 3) into (Equation 4) yields a solution for the time-evolution of the average square of topographic deviations that contains a single roughness element ζ_s ,

$$\langle \zeta_s^2 \rangle(t) = \frac{1}{4\pi^2 H} \int_{-\infty}^{\infty} \int_{-\infty}^{\infty} |\zeta_s(0, k_x, k_y) e^{-Kt[k_x^2 + k_y^2]}|^2 dk_x dk_y, \quad (5)$$

where ζ_s [L] is the topography of a single roughness element (e.g., an individual pit or mound, pit-mound couplet, or mound-pit-mound complex) and H [L or L^2], is the domain size. The topographic roughness, r_s [L^2] is

$$r_s(t) = \langle \zeta_s^2(t) \rangle - \langle \zeta_s(t) \rangle^2, \quad (6)$$

which is the formal definition of the variance of a random variable, and we remind the reader that we use topographic variance to measure the topographic roughness. In the following sections, we demonstrate that if $\zeta_s(x, y)$ can be described by derivatives of Gaussian functions (DoGs), then there are analytical solutions to (Equation 6). More broadly, we suggest that the theory applies to features that can be described as mounds (pits), pit-mound couplets, or mound-pit-mound complexes involve the zero, first, and second-order DoGs, respectively (Figure 2). Furthermore, complex geometries can be represented by summing different DoGs, so the theory applies to many topographic features.

There is a significant overlap between the theory presented in this paper and signal processing. Namely, DoGs are Hermitian wavelets and, most notably, the 2nd order DoG is known as the Ricker Wavelet (Kumar & Foufoula-Georgiou, 1997), which has been used in geomorphology to calculate the low pass-filtered topographic concavity (Lashermes et al., 2007; Struble & Roering, 2021). In Section 4, we generalize the theory to a continuum of topographic forms which resemble a generalized wavelet described in Wang (2015). Despite topographic forms resembling wavelets and our use of the Fourier transform to achieve analytical expressions, we do not use wavelet analysis in this article. However, a similar theory may be achieved by explicitly using a wavelet definition at the outset.

The theory requires that a single process dominates in the creation of topographic roughness for a band of wavelengths because we need to isolate a single roughening rate. This is satisfied in many settings; however, there are notable exceptions that include sources of roughness as legacies of past environments (Del Vecchio et al., 2018) (e.g., solifluction lobes, boulder fields), bedrock exposure (Milodowski et al., 2015), or landslides (Booth et al., 2017; LaHusen et al., 2016) which we avoid. In the settings that we consider, the roughness of the landscape, r , is equal to the sum of all roughness features that have ever existed weighted by a decay function that declines with age due to topographic diffusion. This amounts to a convolution of the rate of roughness production, p [T^{-1}] with the decay function defined in (Equation 3),

$$r(t) = \int_{-\infty}^t p(t') r_s(t-t') dt'. \quad (7)$$

The integral in (Equation 7) clarifies that in these settings, roughness is an archive of past geomorphic events that occurred at time t' . In the context of our four case studies, $p(t')$ is the history of all stochastic events, including desert shrub deaths, tree throw, river avulsions, or impact cratering, that have ever occurred. Insofar as p reflects shrub population dynamics (shrubs), wind or ice storms (tree throw) (Doane et al., 2021, 2023; Hellmer et al., 2015), or trigger events (avulsions) (Martin & Edmonds, 2023), this theory offers potentially valuable information regarding the intersection of geomorphology with ecology and weather. We emphasize the intersection with weather and not climate because we extract information regarding the frequency of discrete events (Doane et al., 2023). In the next sections, we describe theory for specific topographic features.

3. Examples

In this section, we apply the general theory of process topography to several different scenarios in which the Gaussian and derivatives are appropriate approximations. For each example, we define the relevant parameters, appeal to existing literature, and discuss the information that is revealed by process topography. Our intent is to introduce the concept in different contexts and provide a brief description of each setting.

3.1. Zero-Order: Shrub Mounds

In semi-arid environments, vegetation—often woody shrubs—appears in patchy, distributed mosaics separated by swaths of bare soil. Underneath shrubs, small (dm-scale) mounds or topographic highs composed of sediment are observed (Bochet et al., 2000; Furbish et al., 2009; Parsons et al., 1992; Soulard et al., 2012; Worman & Furbish, 2019). As the proposed mechanisms for mound formation are diverse and still debated (Buis et al., 2010; Shachak & Lovett, 1998), we focus here on an accepted, mathematically describable abiotic mound-building process like rainsplash accumulation (Du et al., 2013; Furbish et al., 2009; Parsons et al., 1992). When rain falls in semi-arid settings, the drops impact the bare ground directly adjacent to shrubs at terminal velocity. These discrete impacts drive a radial flux of particles outward from the impact location with some portion of the ejected grains landing beneath shrub canopy, aggrading the sediment mound (Furbish et al., 2009; Parsons et al., 1992). Conversely, the sediment directly under the shrub canopy is protected from rainsplash impact by leaves and branches, halting outward-directed sediment flux from the mound (Furbish et al., 2009; Parsons et al., 1992; Worman & Furbish, 2019). The result of these physical interactions is a net flux of sediment directed toward the shrub, which over time, generates a mound. When the shrub dies, the mound will decay with time as the shrub no longer protects the ground from raindrop impacts. As such, rainsplash-constructed mounds will decay by an approximately diffusive process as the sloping surface drives a net flux outward from the mound (Furbish et al., 2009). This simple, yet physically meaningful interplay of topographic diffusion leads to the realization that topographic roughness of these settings reflects a balance between shrub population dynamics and geomorphic processes. Here, we present theory that clarifies this relationship.

A two-dimensional symmetric Gaussian approximates the mound form described in Furbish et al. (2009) and is

$$\zeta_s(x, y) = A_0 e^{\left(-\frac{x^2}{\lambda_x^2} - \frac{y^2}{\lambda_y^2}\right)}. \quad (8)$$

The mound may be elongated by changing one of the length scales in the exponent, but we consider a symmetric form where $\lambda = \lambda_x = \lambda_y$. Using the topographic form from Equation 8 and following Equations 3–6 we obtain the time evolution of topographic roughness due to a single mound through time as

$$r_s(t) = \frac{\pi A_0^2 \lambda^4}{2H_2(\lambda^2 + 4Kt)} - \left(\frac{\pi A_0 \lambda^2}{H_2}\right)^2. \quad (9)$$

The expected topographic roughness due to all previous shrubs on an entire hillslope is the sum of all mounds of all ages multiplied by the average shrub death rate, S_d [$\# \text{ T}^{-1}$]

$$\mu_r = \frac{S_d A_0^2 \lambda^4 \pi}{8KH_2} \left[\ln\left(1 + \frac{4KT_0}{\lambda^2}\right) - \frac{8\pi KT_0}{H_2} \right] \quad (10)$$

where

$$T_0 = \frac{1}{4} \left[\frac{H_2}{2\pi K} - \frac{\lambda^2}{K} \right] \quad (11)$$

is a saturation timescale that reflects the time for a single feature to diffuse across the domain, H_2 . The total topographic roughness of a hillslope at any moment also involves the mounds under live shrubs, which is the initial condition for diffusing mounds. Adding these terms together,

$$\mu_r = S_a \frac{A_0^2 \lambda^2 \pi}{2H_2} \left[1 - \frac{2\pi \lambda^2}{H_2} \right] + \phi_d S_a \frac{A_0^2 \lambda^4 \pi}{8KH_2} \left[\ln\left(1 + \frac{4KT_0}{\lambda^2}\right) - \frac{8\pi KT_0}{H_2} \right], \quad (12)$$

where the first term describes the topographic roughness due to active mounds and the second term describes the roughness due to decaying mounds. The term ϕ_d [T^{-1}] describes the fraction of live shrubs that die per unit time so that $\phi_d S_a = S_d$, where S_a [$\#$] is the number of live shrubs. Estimating values for K remains a challenge in

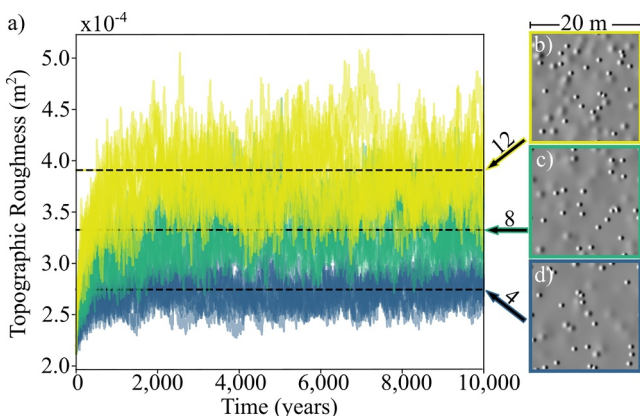


Figure 3. (a) Time series for equal live shrub spatial density (550 per Ha), but with turnover rates of 4 (blue), 8 (green), and 12 (yellow) shrub deaths per year per hectare per year. Each model with a specified turnover rate was run 5 times to illustrate the central tendency of the roughness to oscillate around the expected value which is plotted with the straight lines. Topographic roughness reflects two shrub subpopulations: growing mounds under live shrubs and decaying mounds under dead shrubs. Each shrub that dies per year is replaced. Dotted lines are theoretical predictions from Equation 12. (b–d) Corresponding hillshades of resulting topography.

geomorphology and it varies over a couple orders of magnitude. However, previous work suggests that K is a function of climate (Madoff & Putknoonen, 2016, 2022; Richardson et al., 2019) or, in the case of rainsplash, it can be developed with theory (Furbish et al., 2009). Further, Doane et al. (2021, 2023) demonstrate that meaningful statistical information can be extracted without knowing exact values of K .

We numerically simulate a topographic surface that accumulates shrub mounds which diffuse through time. The relevant parameters include A_0 and λ , which relate to mound sizes (Furbish et al., 2009), and S_a and ϕ_d , which relate to shrub spacing and lifespan statistics (Gearon & Young, 2020). Shrub spacing may vary depending on aspect, climate, and species; but two meters appears to be a reasonable estimate (Gearon & Young, 2020). This corresponds to roughly 550 shrubs per hectare and is consistent with Worman and Furbish (2019). For each run in our model, the number of shrubs that die is held constant through time and each shrub that dies is replaced by a new one. We test simulations where shrub deaths are randomly selected with an average 4, 8 and 12 shrub deaths per year per Ha. These rates correspond to 0.7%, 1.4%, and 2.1% of shrubs dying per year. Results from the numerical model demonstrate that theory matches the numerics (Figure 3) and that the expected topographic roughness scales linearly with the number of shrubs that die per year. Or, said another way, shrub populations with faster turnover create rougher surfaces (Figure 3). Because we randomly select the for shrub deaths, the variance of roughness also grows with the increased turnover.

Previous field observations are consistent with this theory. Soulard et al. (2012) measure topographic roughness due to mounds under shrubs in burned and unburned plots of land. Burning occurred a decade prior to the measurement, which removed shrubs from the landscape and left mounds vulnerable to erosion by rainsplash or wind. Those authors demonstrate that the unburned plots were rougher because of the consistent shrub cover compared to the recovering shrub cover in the burned section.

Equation 12 contains many parameters. However, most of them are measurable with a simple field campaign. The only unknowns are K , the topographic diffusivity, and ϕ_d , the portion of shrubs that die in any given year. Isolating either variable and rearranging Equation 12 allows for the recovery of the other one. For example, comparing the unburned and burned plots from Soulard et al. (2012) enables one to back out a representative K value because the spatial density of live shrubs is known a priori and post-burn measurements allows for the decay of roughness over time due to topographic diffusion. The inverse may also be achieved. If one knows or can estimate the topographic diffusivity, then one may be able to back out the population dynamics or time since a major disturbance. We note that applying Equation 12 in these ways requires some assumptions; however, the theory suggests that there is specific process-based information in topographic roughness.

3.2. First Order: Pit-Mound Couples

Tree (or wind) throw is a natural ecological disturbance to forests that occurs when an external force exceeds the strength of roots, soil, and rock (Gardiner et al., 2016; Hellmer et al., 2015; Phillips et al., 2017; Šamonil et al., 2019) (Figure 4). The external force is often extreme wind gusts or snow and ice loading on the canopy. When this happens, trees uproot which mixes and transports soil (Gabet et al., 2003; Hellmer et al., 2015; Norman et al., 1995), creates ecological niches, removes carbon from the above-ground carbon stock (Lindroth et al., 2009), affects hydrologic pathways (Valter & Schaetzl, 2017), and leaves a topographic signature of a pit-mound couplet (Doane et al., 2021). With time, slope-dependent sediment transport processes tend to degrade the topographic signature such that old couplets have a muted expression and return toward a flat surface.

The forces required to uproot live trees usually occur during extreme atmospheric events (Cannon et al., 2017; Gardiner et al., 2016; Godfrey & Peterson, 2017; Lindroth et al., 2009) which have recurrence intervals that are long relative to human timescales such that direct observation of these events is challenging. In previous work, Doane et al. (2021) developed theory that describes the expected topographic roughness of forests that are subjected to tree throw and interprets roughness as the balance between tree throw frequency and creep-like

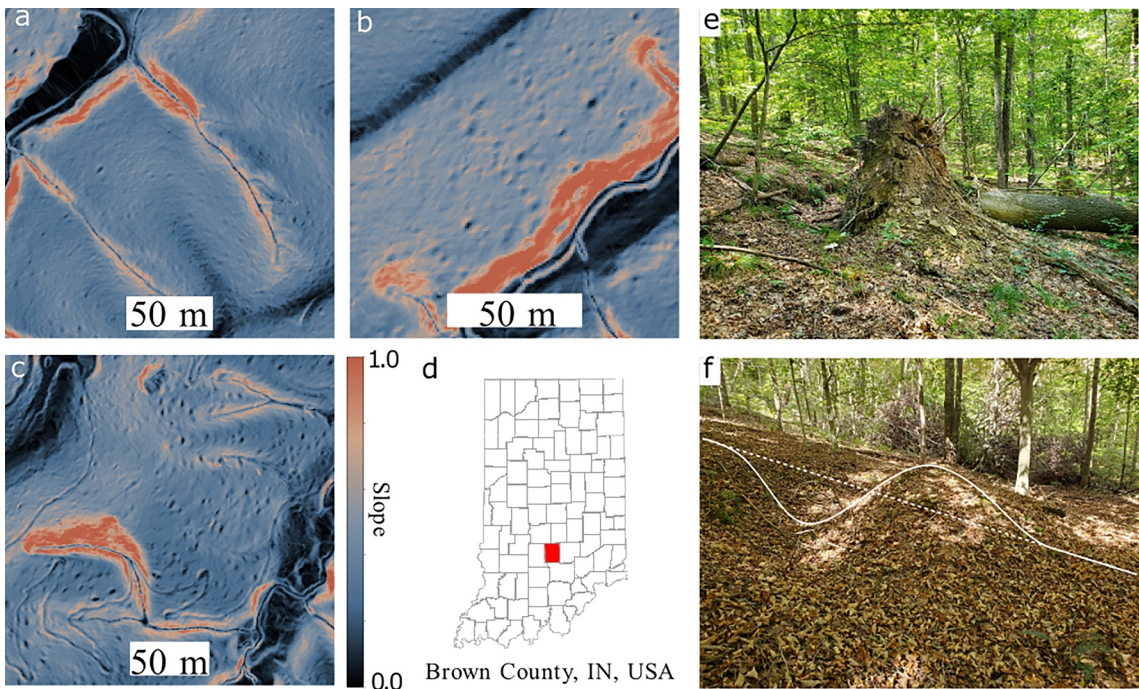


Figure 4. Three different slope maps from three hillslopes in southern Indiana illustrating different spatial concentrations of tree throw as a process (a–c). Each pock mark on the slope map is an individual pit-mound couplet and adds roughness to the surface. (d) The location of Brown County in southern Indiana. (e) A fresh tree throw event with the roots and tree still intact and (f) an older couplet that has turned into a pit-mound couplet.

processes (Doane et al., 2021, 2023). In those papers, the authors conduct similar analyses and modeling efforts to what we have done here in the previous and following sections. We refer readers to those articles for a thorough discussion, and we instead focus on the underlying theory in this article.

The initial condition for tree throw pit-mound couplets are approximated by

$$\zeta(x,y) = \frac{2A_1 x}{\lambda_x^2} e^{\left(-\frac{x^2-y^2}{\lambda_x^2 \lambda_y^2}\right)}, \quad (13)$$

which is the product of a zero-order DoG in the y -direction and a first-order DoG in the x -direction (Figure 2). Doane et al. (2021) demonstrates that the topographic roughness of a single pit mound couplet decays as

$$r(t) = \frac{A_1^2 \lambda_x^2 \lambda_y^2 \pi}{32 H_2} \left[\frac{\lambda_x^2}{4} + Kt \right]^{-\frac{3}{2}} \left[\frac{\lambda_y^2}{4} + Kt \right]^{-\frac{1}{2}}. \quad (14)$$

The topographic roughness of an entire hillslope is the sum of all pit-mound couplets that have ever occurred, weighted by their age according to (Equation 15),

$$r(t) = C \int_{-\infty}^t p(t') \left[\frac{\lambda_x^2}{4} + K[t-t'] \right]^{-\frac{3}{2}} \left[\frac{\lambda_y^2}{4} + K[t-t'] \right]^{-\frac{1}{2}} dt', \quad (15)$$

where C is the leading fraction in (Equation 14). In many cases, $\lambda_x \approx \lambda_y$ so that the integral simplifies to,

$$r(t) = C \int_{-\infty}^t p(t') \left[\frac{\lambda^2}{4} + K[t-t'] \right]^{-2} dt'. \quad (16)$$

A key result from Doane et al. (2021) solves for the expected topographic roughness,

$$\mu_r = \frac{A_1^2 \lambda_x^2 \pi}{4[\phi_{pm}^2 - \phi_{pm}] H_2} \frac{\mu_p}{K}, \quad (17)$$

where $\phi_{pm} = \frac{\lambda_x}{\lambda_y}$ is the aspect ratio of the couplet and Equation 17 has the same form as (Equation 1). Doane et al. (2021) use Equation 17 to estimate the ratio of sediment fluxes due to tree throw versus slope-dependent creep-like processes in Indiana and Doane et al. (2023) use Equation 15 to identify the probability distribution of tree throw frequency in Indiana. In the latter article, the authors solve for the variance of topographic roughness values, and then, using measured roughness values from a county in southern Indiana, suggest a form for the probability function of wind throw production rates, p , which is a random variable of the number of trees to fail per hectare per year. Those authors further relate that probability function of wind throw frequency to the distribution of extreme winds in southern Indiana that likely drive the bulk of tree throw events. That study is an example of the type of process-based information that is revealed by a detailed study of topographic roughness.

3.3. Second Order: Channel Levees and Craters

Avulsions are abrupt changes in the location of river channels onto the adjacent surface and they are a key process in controlling how alluvial landscapes evolve (Slingerland & Smith, 2004). When a new channel is emplaced, a river usually incises a trench-shaped depression into a floodplain or fan surface that, when viewed perpendicular to flow direction, resembles a pit and is reasonably described by a zero-order DoG. As the channel continues to evolve, sediment preferentially deposits in and near the channel, such that rivers build levees and alluvial ridges (Gearon et al., 2024; Hajek & Wolinsky, 2012), which are positive topographic features. These mound-pit-mound features may be reasonably described by a second-order DoG. After an avulsion, rivers leave behind their abandoned channel-levee complexes (assuming they do not get immediately filled with sediment) which create topographic roughness across floodplains and fans and will evolve by two processes: creep-like processes and channel filling processes during floods (Pelletier & Turcotte, 1997). We present theory for slope-dependent processes in the main text and demonstrate the effect of channel filling processes such as deposition during floods in Supplemental Information.

Avulsions are infrequent and rarely observed directly. This limits avulsion studies to the past several decades of remote sensing (Brooke et al., 2022; Edmonds et al., 2016; Valenza et al., 2020), case studies of Holocene-era avulsions (Berendsen & Stouthamer, 2002), stratigraphic records that contain more ambiguous information but are extensive archives in time (Hajek & Edmonds, 2014; Mohrig et al., 2000), or experiments that are informative but operate over different scales than nature (Reitz & Jerolmack, 2012). We argue that topographic roughness has potential to be an informative metric for establishing the historic frequency of avulsions based on resulting topography, letting modern landscapes serve as archives over centuries to millennia of channel history. Our theory presents a first-order time-evolution of topographic roughness of fans. It can incorporate a continuum of channel shapes from un-leveed to having pronounced levees and alluvial ridges. This theory may be improved upon by considering the effects of heterogeneous material and channel reoccupation (Hajek & Edmonds, 2014; Martin & Edmonds, 2022; Reitz & Jerolmack, 2012) more directly.

The theory is most directly applicable to active fans where channels commonly reroute due to frequent avulsions. Previous researchers have considered the roughness of alluvial fans to establish a relative age dating method for abandoned surfaces (Frankel & Dolan, 2007; Johnstone et al., 2018). Johnstone et al. (2018) in particular develop theory that takes advantage of similar mathematical relationships. The theory presented here is slightly different in that we assume an idealized initial condition and solve for the time-series of the roughness using the entire Fourier series. This allows us to address the roughness of active surfaces as opposed to the age of abandoned surfaces as done in Johnstone et al. (2018).

We begin with the case of channels without levees (i.e., that can be approximated by a one-dimensional negative Gaussian) which is a one-dimensional problem in the cross-channel direction,

$$\zeta_s(x) = -A_0 e^{-\frac{x^2}{\lambda^2}}, \quad (18)$$

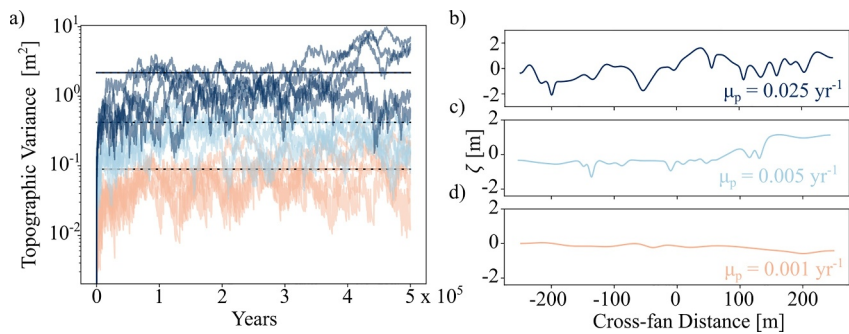


Figure 5. (a) Time series of topographic variance along a profile for three different avulsion frequencies (0.025, 0.005, 0.001 per year for the 500 m-wide contour). (b–d) Examples of detrended topographic profiles for the three avulsion frequencies and a diffusivity of $K = 0.05$.

The time-evolution of the topographic variance of a single channel is

$$r_s(t) = \frac{\sqrt{\pi}A_0^2\lambda^2}{2H_1\sqrt{2}} \left[\frac{\lambda^2}{4} + Kt \right]^{-\frac{1}{2}} - \frac{\pi A_0^2\lambda^2}{H_1^2}, \quad (19)$$

Where H_1 [L] is the domain length. Note that Equation 19 is valid up to some finite time, T_0 , which is when the first term on the right-hand-side equals the magnitude of the second,

$$T_0 = \frac{\lambda^2}{4K} \left[\frac{H_1}{2\pi\lambda} - 1 \right]. \quad (20)$$

The quantity $\lambda^2/(4K)$ is a diffusive timescale for the channel. The parenthetical part states how many diffusive timescales it takes for the feature to diffuse across the domain length, H_1 , to a negligible topographic feature. Equation 19 describes the evolution of topographic roughness for an abandoned channel that only evolves by creep-like, diffusive processes that rearrange the sediment. The topographic roughness of a surface involves the sum of all channels of all ages up to T_0 which is accomplished by integrating over the system's history (Equation 7) and the result is

$$\mu_r = \mu_p \left[\frac{A_0^2\lambda^2}{K} - \frac{\sqrt{2\pi}A_0^2\lambda^3}{KH_1} - \frac{\pi A_0^2\lambda^4}{4H_1^2K} \left[\frac{H_1^2}{2\pi\lambda^2} - 1 \right] \right], \quad (21)$$

where μ_p [<# T⁻¹] is the average frequency of avulsions.

We numerically simulate the topographic profile that runs perpendicular to the flow direction. A reasonable environmental analog would be a fluvial or alluvial fan. Our numerical model simulates each avulsion by randomly emplacing a channel with a predefined geometry, $\zeta_s(x)$, at a position x_0 along a contour of a 500 m-wide profile or fan at a frequency of 0.025, 0.005, and 0.001 avulsions per year. There are no rules that control the location of channel emplacement, so if a new channel overlaps with an older one it will overprint the depth, and the shape will be the union of the two shapes. An abandoned channel may be partially diffused before it is overprinted, which means that topography is only marginally affected by the overprinting. With this rule in place, the numerical roughness is expected to be less than the theoretical, and this effect should be greater for systems with more frequent avulsions. Indeed, Figure 5 shows that theory matches numeric results, but begins to diverge for larger values of p/K . However, for low avulsion rates, theory matches numerics.

We now turn to channel-levee complexes, which are mound-pit-mound features that involve the second derivative of the Gaussian (Figure 2). To capture the full range of the relative magnitudes of levees (alluvial highs) as compared to the channel depth, we describe the cross-section of a river as a sum of the zero and second order DoGs,

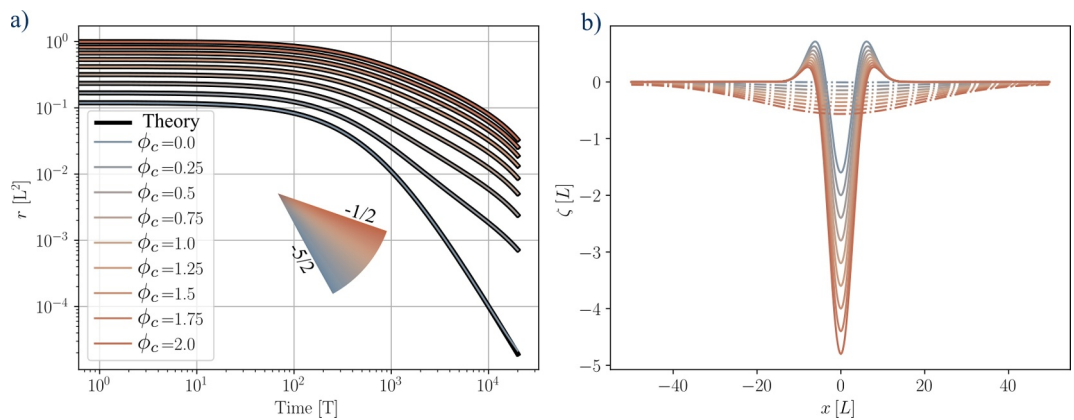


Figure 6. (a) Topographic roughness, r , for different values of ϕ_c through time and (b) topographic representation of the initial condition (solid line) and after 20k years (dot-dash) of diffusion with $K = 0.01$.

$$\zeta_s(x) = -A_0 e^{-\frac{x^2}{\lambda^2}} - A_2 \left[\frac{4x^2}{\lambda^4} - \frac{2}{\lambda^2} \right] e^{-\frac{x^2}{\lambda^2}}, \quad (22)$$

where A_0 [L] and A_2 [L^2] are amplitudes of the two functions. Figure 6b (solid lines) shows topographic forms composed of various combinations of amplitudes for zero and second-order DoGs. For reference, the magnitude of minima of these functions are equal when $A_2 = -\frac{A_0^2 \lambda^2}{2}$. Following through with the steps described in section (Equation 2), we solve for the decay of topographic roughness through time for a single channel-levee complex. This shows that r decays at different rates that depend on the ratio, $A_0 \lambda^2 / [2A_2] = \phi_c$,

$$r(t) = \frac{\sqrt{\pi} \lambda^2 A_2^2}{32 \sqrt{2} H_1} \left[\left[\frac{8\phi_c}{\lambda^2} \left[\frac{\lambda^2}{4} + Kt \right] + 1 \right]^2 + 2 \right] \left[\frac{\lambda^2}{4} + Kt \right]^{-\frac{5}{2}} - \frac{\pi 4 \phi_c^2 A_2^2}{H_1^2 \lambda^2}. \quad (23)$$

Note that when $\phi_c = 0 = A_0$, the first term in Equation 23 simplifies to $C \left[\frac{\lambda^2}{4} + Kt \right]^{-5/2}$, where C is the leading fraction on the right-hand side of (Equation 23). As ϕ_c increases, the rate of decay of topographic variance approaches that of a channel without a levee ($r \propto t^{-1/2}$ Figure 6a). To ensure that our theory is correct, we plot the theoretical decay of variance for different values of ϕ_c in Figure 6a and the topographic forms that they decay toward in Figure 6b. Equation 23 could then be convolved with the history of avulsions for a channel with any initial conditions.

Equation 23 is a general description of topographic roughness for many channels. Natural channels that achieved different levels of aggradation before abandonment should have formed along a continuum from having no levees to those that might be approximated by the second derivative of a Gaussian alone ($\phi_c = 0$) (Adams et al., 2004; Mohrig et al., 2000). In addition to considering topographic roughness along fans, a similar theory might apply to abandoned channels resulting from meander cutoffs along meandering channels. However, our theory as presented neglects any accumulation in abandoned channels by overbank flow (Hajek & Wolinsky, 2012). Such a process could be incorporated into (Equation 24) with a term that accounts for the bulk reduction in variance from deposition in existing lows. In Supporting Information S1, we present results from a numerical model that includes infilling from overbank flows, which deviates from theory by an amount that depends on the pace of infilling and the magnitude of K . Numerical simulations demonstrate that flood deposition quickens the decay of variance by an amount that scales nonlinearly with λ/K , where v is the average rate of deposition in the lows (Supporting Information S1). The interplay of these two processes warrants deeper investigation.

We present a brief case study from the San Luis Valley, CO, USA. The alluvial fans of this valley emerge from the western front of the Sangre De Cristo Range which is bound by a normal fault (Ricketts et al., 2016). We explore the down-fan trend in topographic roughness to illustrate how it can be interpreted as a proxy for relative avulsion frequency. We do not parameterize this model, and instead present it only as an example and interpret the results

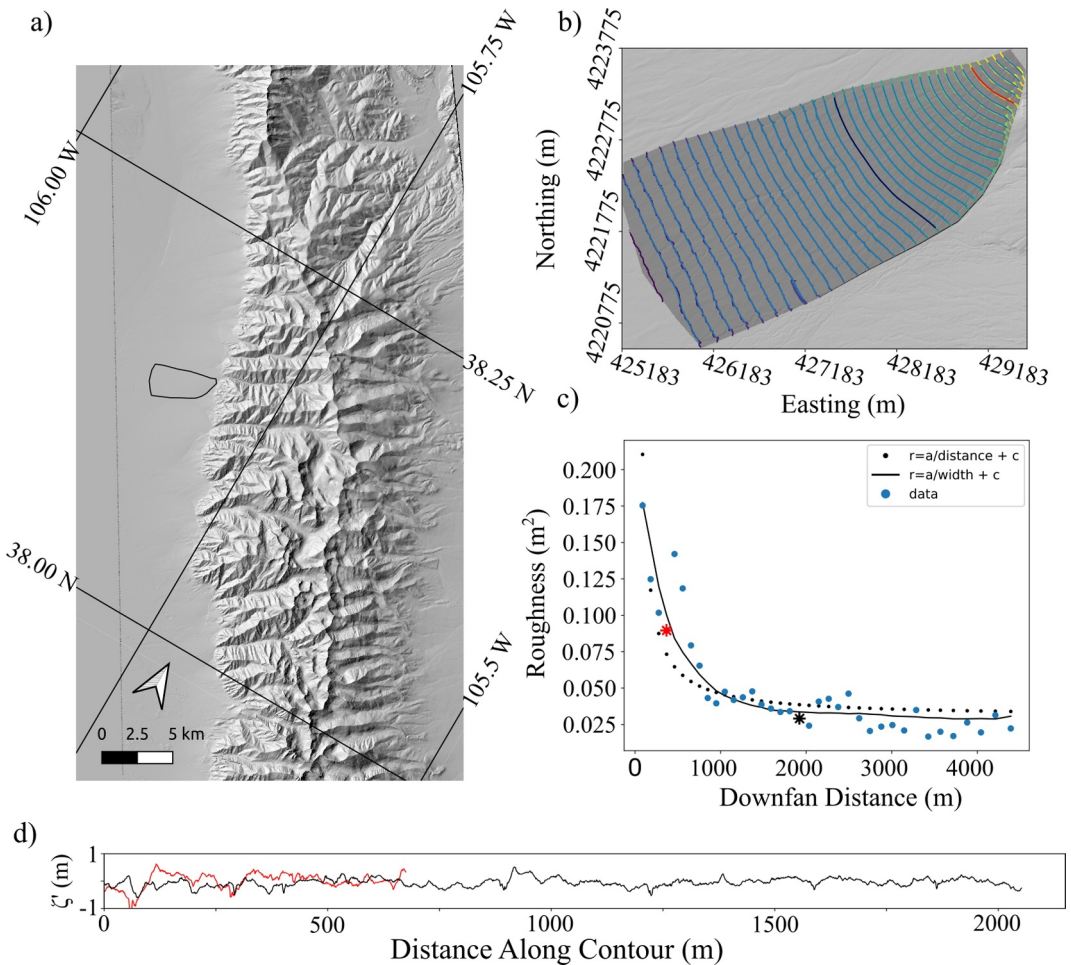


Figure 7. (a) Hillshade of the Sangre de Cristo Range in Colorado, USA, with the location of the alluvial fan outlined. (b) Hillshade and contours of an alluvial fan along the west front of the Sangre de Cristo Range. Blue lines are smoothed contours that are the locations of topographic profiles that we use to calculate topographic variance. Colored lines behind blue lines are the original unsmoothed contours. (c) Topographic roughness declines as a function of down-fan distance with fit functions relating roughness to fan width and downslope distance. (d) Example of detrended topographic profiles along topographic contours which correspond by color with data in panels (b, c).

broadly. This fan lacks any elevated or obviously abandoned surfaces (Johnstone et al., 2018) and we interpret the entire surface to be active. Topographic roughness is measured along profiles that are extracted from LOESS filters (Seabold & Perktold, 2010) of topographic contours, such that each profile is detrended to remove the large-scale topography of the fan while retaining the topography resulting from individual channels.

Figure 7 illustrates that topographic roughness declines nonlinearly with down-fan distance on one fan in the San Luis Valley. Equation 21 predicts a linear relationship between topographic roughness and avulsion frequency, in terms of number of avulsions per time per unit length. Therefore, a nonlinear decline in topographic roughness with distance down-fan, could indicate a nonlinear decline in avulsion frequency. We explore two potential geometrical arguments that explain the nonlinear decline in avulsion frequency as indicated by topographic roughness. First, in this setting, debris flows that build the fan may rarely reach the base, resulting in less channel relief. For such a case, we may expect topographic roughness to decline inversely with down-fan distance. Alternatively, declining down-fan roughness may be a consequence of fan widening. If we assume that most or all avulsions occur near the apex of the fan, then each contour has the same probability of an avulsion occurring on it. However, wider parts of the fan would have a lower frequency per unit width, which would cause topographic roughness to decline inversely with fan width. In this case, both descriptions appear to fit the data well, and we

cannot discriminate between the mechanisms for down-fan smoothing. This study warrants a deeper field investigation, and we present this case as an example of how one might use information encoded in alluvial fans.

3.4. Impact Craters

Topographic roughness of planetary bodies other than Earth has been used to map processes and geologic units of Mars (Campbell et al., 2013; Cao et al., 2023; Orosei et al., 2003), the moon (Cai & Fa, 2020; Guo et al., 2021; Kreslavsky et al., 2013), and Mercury (Kreslavsky et al., 2014). In some cases, these bodies, or selected surfaces on them, are primarily sculpted by impact cratering. Impact craters have a mound-pit-mound geometry, which should be describable by a 2nd-order DoG, and the theory presented here should apply. Furthermore, impact craters are ideal morphologic features for this theory because they are remarkably consistent in their form (Fassett & Thomson, 2014). The moon is well-suited because there are few geomorphic processes at work on the surface and the primary one (micrometeorites) leads to diffusive-like evolution of topography (Fassett & Thomson, 2014). Indeed, Fassett and Thomson (2014) describe the topographic evolution of lunar craters with linear diffusion and develop a relative age-dating technique.

In addition to topographic roughness, there is a rich legacy of crater-counting studies on planetary bodies (Gault, 1970; Melosh, 1989; Xiao & Werner, 2015). These studies generally focus on probability distributions of crater size for given areas, which can ultimately be used as a relative or absolute age-dating technique. In those studies, researchers are limited to a binary metric in terms of whether there is a well-resolved crater or not. We see our theory as providing an alternative measure with topographic roughness being explicitly a function of cratering, which does not require the individual counting of craters and only relies on topographic data. A complete study that explores the relationship between roughness and different distributions of crater sizes is beyond the scope of this study. Instead, we intend to illustrate how our theory applies and briefly present some data.

The initial condition is provided by Fassett and Thomson (2014), who identify an idealized empirical expression for the initial condition of an impact crater. We represent the topography as the best-fit sum of a zero and second order Gaussian to the form provided by Fassett and Thomson (2014). This is because the second order DoG alone would create crater rims that are roughly half the amplitude of the depth of the crater. In reality, craters are much deeper than their rims are high and so we add a zero-order DoG increase the depth to the correct form. Fitting the sum of DoG's to Fassett and Thomson's (2014) expression we note the following relationships,

$$A_2 = A_0 \lambda^2 / 2,$$

$$A_0 = 0.19R,$$

$$\lambda = 0.85R,$$

which are consistent for many craters with radial distance to rim, R [L] (Fassett & Thomson, 2014).

Our goal is to determine the analytical solution for the evolution of topographic roughness of a diffusing crater. However, the craters are two-dimensional features, and their geometry is best described as a sum of two DoGs. Given that a calculation of topographic roughness involves squaring topography and integrating, the number of terms in an analytical solution quickly becomes unwieldy. Instead, we observe that in all cases presented above, the decay term involves the quantity $(\lambda^2/4 + Kt)^{-\alpha}$ where α depends on the geometry of the feature (mound, pit-mound, mound-pit-mound). There are then two ways to describe the initial topographic roughness of a crater. First, we can empirically determine a function for the form provided by Fassett and Thomson (2014) which turns out to be,

$$r(t=0) = \frac{0.09R^4}{H_2} - \frac{0.0484R^6}{H_2^2}. \quad (24)$$

Or second, we can solve for the roughness of the initial condition of the combination of Gaussian functions that is a best fit to the form from Fassett and Thomson (2014).

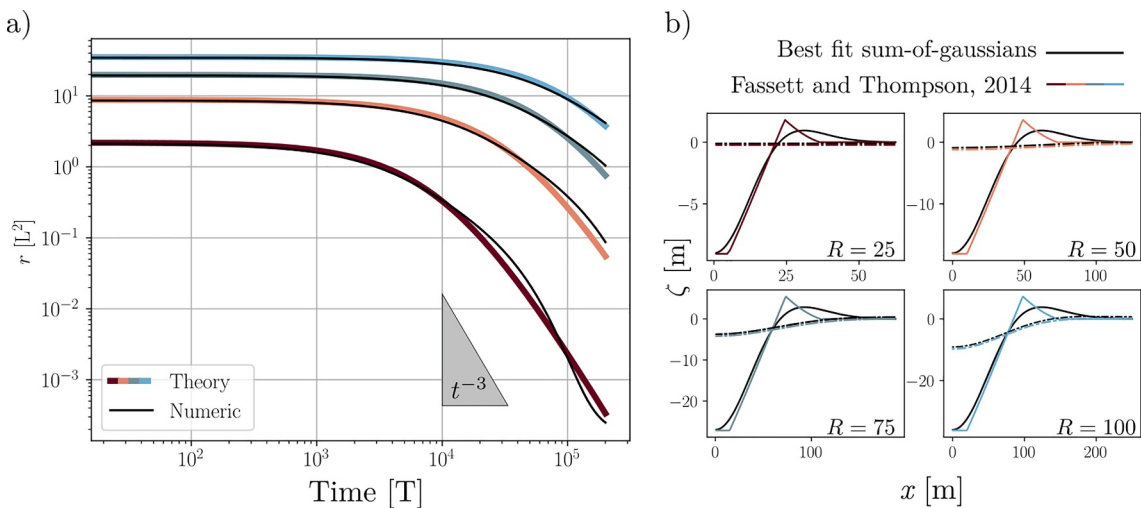


Figure 8. (a) Numerical and quasi-theoretical (Equation 26) evolution of topographic roughness for four craters of different radii, R . (b) Four different craters of different radii with the initial form given by Fassett and Thomson (2014) in colors and the best-fit sum-of-gaussians to that form shown in black. The diffusion of those both form is shown in the dash-dot lines after equal amounts of time.

$$r(t=0) = \left[\frac{\pi A_0^2 \lambda^4 + 4A_2^2}{2H_2 \lambda^2} - \frac{\pi^2 [A_0 \lambda^2 - 2A_2]^2}{H_2^2} \right]. \quad (25)$$

Last, numerical experiments illustrate that for this topographic form, $\alpha = 3$ so that we suggest

$$r(t) \approx r(0) \left[1 + \frac{4Kt}{\lambda^2} \right]^{-3}, \quad (26)$$

And $r(0)$ can be represented by either Equations 24 or 25. Figure 8a illustrates that Equation 26 matches numerical experiments run on craters of different sizes (Figure 8b).

The cumulative roughness due to craters of a certain size is the integral of all impacts through time,

$$r(t, R) = r(0, R) \int_{-\infty}^t p(t', R) \left[1 + \frac{4K[t-t']}{\lambda^2} \right]^{-3} dt'. \quad (27)$$

Note that this is roughness due to craters of a certain size, R . For the purpose of this paper, we do not consider the consequence of crater overprinting, in which young large craters obliterate and cover the signal of older smaller craters. Overprinting could be incorporated into the theory by removing some portion of craters of size R with a frequency that relates to that of all larger craters. There is a large body of research that investigates the probability functions of crater sizes around the lunar surface (Fassett, 2016; Gault, 1970; Melosh, 1989; Xiao & Werner, 2015) which largely suggest that crater sizes on the moon are distributed as a power-law with $f(R) \propto R^{-2}$, where $f(R)$ is the probability density function of crater sizes that are in statistical equilibrium. In particular, we note Gault's definition that equilibrium is a state achieved when the crater production and degradation processes are equal—regardless of the degradation process. Gault was counting individual craters, so their definition applied to features that were visible. By using topographic variance, we do not need to qualify whether or not a crater is visible as very old craters contribute very little to the variance. Topographic variance, framed in this way, may complement crater counting studies that focus on identifying conditions for crater saturation or equilibrium.

We briefly examine the topographic roughness from high-pass filters of the lunar Highlands using a 2-m resolution DEM from the Lunar Reconnaissance Orbiter Camera Digital Terrain Models (Henriksen et al., 2017) and a Gaussian kernel of different length scales, λ_c (Figure 10b). The difference between two successive high pass-

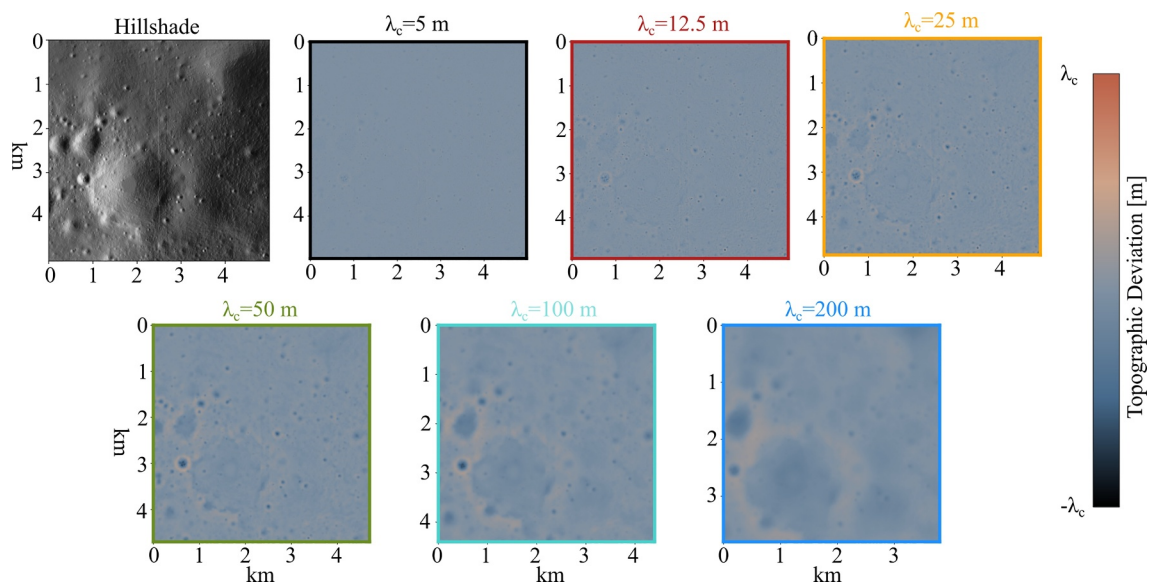


Figure 9. Hillshade and band-pass filters generated from 2-m resolution lunar topography and filtered by Gaussian filters with an upper length scale of λ_c . Area is located at approximately 43.43°N, 167.95°E, in the Lunar Highlands. Colors bounding the subfigures relate to colors in Figure 10.

filters highlights topography at a certain scale ($\lambda_c - \lambda_{c-1}$). The topographic roughness is calculated as the variance of this band-passed topography. To be clear, λ_c refers to the upper bound of the band's length scale. Across six different bands of crater size, we identify a power-law relationship between the topographic variance and the smoothing scale where $r \propto \lambda_c^2$ (Figure 9a). We emphasize that this measure of roughness is for only a band of wavelengths, meaning that it is the difference between two high-pass filters and, therefore, only highlights the topography of a given scale (Figure 9b).

The power law relationship of $r \propto \lambda_c^2$ generally agrees with published data statistical representations of surface roughness. Cai and Fa (2020) conducted a similar analysis on the same data and found that the standard deviation of elevation for detrended topography varied as $\lambda_c^{0.88}$, where 0.88 is the Hurst exponent and λ_c is the length scale of a moving average. Our analysis of a small section of the lunar Highlands suggests a similar relationship with RMS (square root of r) varying approximately linearly with λ_c , which is similar to Cai and Fa (2020). However, we note that our analysis only considers a band of roughness between two length scales as opposed to all contributions to roughness at length scales shorter than a λ_c .

Theory in this paper provides a method for understanding the interplay between impact rates and topographic smoothing, which is absent from many crater counting studies. We have not attached any numbers to the analysis

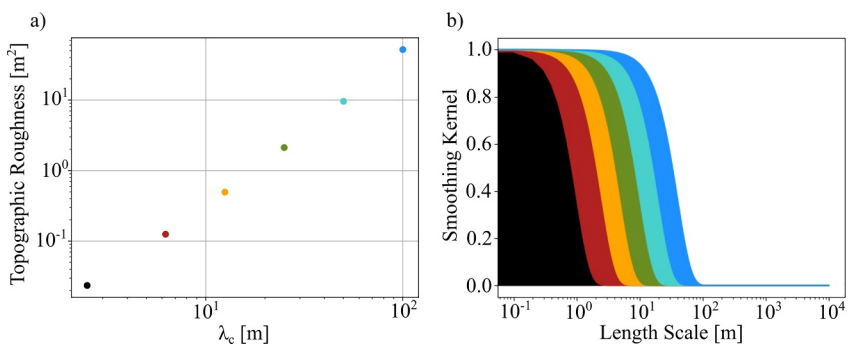


Figure 10. (a) Topographic roughness measured for craters with length scales in the bands shown in panel (b). Note that Cai and Fa (2020) plot the standard deviation as a function of measurement length scale. Taking the square root of variance would reduce the slope (Hurst exponent) of the line in panel (a) from about 2 to 1. Colors relate to subfigures in Figure 9.

here because it is beyond the scope of this paper. However, one could use this theory to either determine impactor rates through time or topographic diffusivity. One interesting note is that we may expect there to be a scale-dependent diffusivity on the moon because larger craters will diffuse by the action of all smaller meteorites. Therefore, as craters increase in size then there are more impactors that act to diffuse topography over smaller scales, which in turn increases the topographic diffusivity. We emphasize that this recalls our statement in the introduction whereby topographic roughness elements decay by the action of all processes that operate over smaller scales (Figure 1). In the case of lunar topography, all smaller impactors degrade larger ones.

Now that we have collected results for several different natural features, we turn to a generalization of the theory. Further, we identify characteristic timescales for the decay of topographic roughness for different features.

4. Generalization

The previous sections describe theory that is specific to several different processes. Here, we collect those results and specify patterns that we have observed and generalize so that the theory is relevant to a range of initial conditions, sediment transport behaviors, and temporal characteristics of noisy roughening processes (shrub deaths, tree throw, avulsions, cratering).

4.1. Generalizing Geometry

We begin with a generalization of the decay function for a continuum of initial conditions. The theory differs for each initial condition; however, each version contains a term with $\left[\frac{k^2}{4} + Kt\right]^{-\alpha}$, where the values of α vary by feature. There is a pattern in the value of α that depends on the order of the derivative n and the feature dimensionality, D_N ,

$$\alpha = \left[n + \frac{1}{2} \right] D_n. \quad (28)$$

In the case where an initial condition is a sum of two different derivatives, the decay rate is weighted by their contributions to the function. For example, the contributions to the variance of a crater are almost equal between the zero and second derivative of the Gaussian and dimensionality, $D_n = 2$. In that case, a zero order DoG has variance that decays as t^{-1} and the second order DoG has topographic roughness that decays as t^{-5} . Because both of those functions contribute equally to the crater form, we take their average and $\alpha = (1 + 5)/2 = 3$. Furthermore, this pattern extends to non-integer orders of DoG which add some asymmetry to the features and may be more realistic in certain settings (Figure 11a). Equation 28 allows for the generalization of the specific idealized examples to a continuum of initial conditions for features. Examples of features that are well-described by a non-integer DoG are tree throw pit-mound couplets on shallowly sloping topography (Doane et al., 2021) or asymmetric levees along a channel.

Even though our theory can produce a continuum of initial conditions, natural features may still differ from those geometries. Notably, topographic variance is a robust measure of roughness and the theory applies even for features that differ slightly from the exact forms. So long as a feature can be described as a pit, pit-mound couplet, or mound–pit–mound complex, the theory applies. To demonstrate this, we numerically diffuse other initial conditions that are constructed from boxes or triangles. Figure 12 shows that although the shapes differ, features described as a pit, pit-mound couplet, or mound-pit-mound complex in one dimension will have variances that decay approximately as $t^{-1/2}$, $t^{-3/2}$, and $t^{-5/2}$ respectively.

4.2. Generalizing Transport

We also extend the theory to include nonlocal sediment transport models which are a relatively new class of sediment transport models for geomorphology (Foufoula-Georgiou et al., 2010; Furbish & Haff, 2010; Furbish & Roering, 2013; Tucker & Bradley, 2010). Theory developed above relies on a local description of the sediment flux. That is, the sediment flux at a position x is only a function of conditions at position x . A nonlocal formulation allows for the possibility that the sediment flux at location x is a function of conditions surrounding x as well, which acknowledges that particles travel finite distances. The impact of nonlocal formulations is greatest on steep topography where particles travel long distances (DiBiase et al., 2017; Roth et al., 2020) or where particle travel

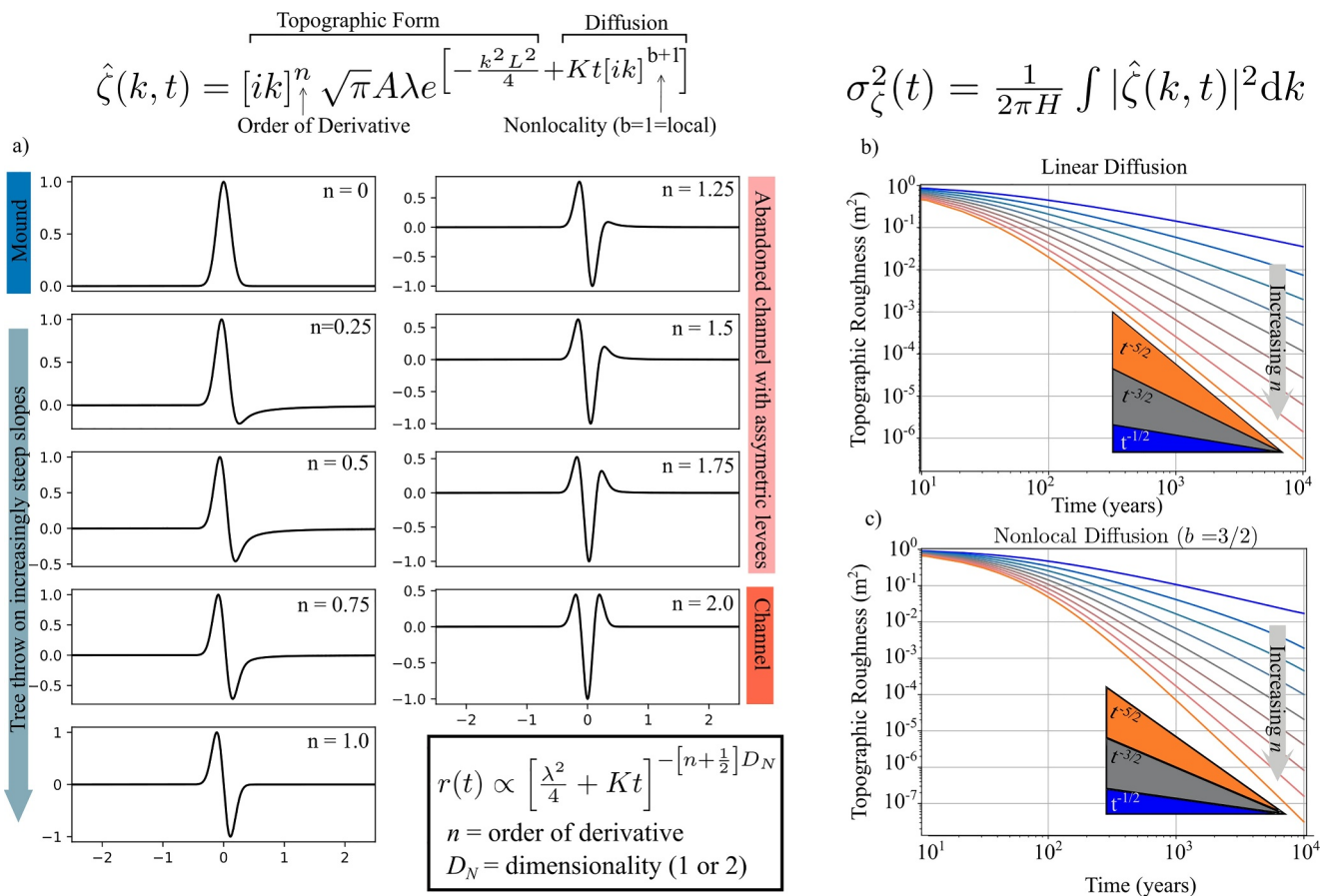


Figure 11. (a) Generalization of the Gaussian and its fractional derivative forms, which allows us to represent a wide range of natural features. Using the two equations at the top of the figure, we achieve a solution for the decay of topographic variance for all forms according to local linear diffusion (b) and nonlocal diffusion by using fractional derivatives for the evolution of the feature (c). For the case of linear diffusion, variance decays as a nonlinear function that depends on the order of the derivative of the Gaussian, n , and the dimensionality of the feature (1 or 2 dimensions).

distances are long relative to the spatial scale over which conditions change (Furbish et al., 2021). In the case of roughness elements, features are small and particle travel distances may be long relative to feature length scales. For example, mounds under shrubs will decay by rainsplash, for which particle travel distances can approach decimeters (Furbish et al., 2009). In this case, a nonlocal description may be appropriate to describe the decay of shrub mounds because particle travel distances are similar to the scale of the feature. Or alternatively, the initial evolution of an abandoned channel may involve particles raveling down steep surfaces which would be better described by nonlocal sediment transport. The most relevant condition for sediment transport is the land-surface slope, $d\zeta/dx$ and one way to incorporate nonlocality is through fractional calculus (Foufoula-Georgiou et al., 2010; Ganti et al., 2012; Schumer et al., 2009), which writes the sediment flux as a function of a non-integer derivative of the land surface,

$$q \propto \frac{d^b \zeta}{dx^b}, \quad (29)$$

where $0 < b \leq 1$. The theory presented above is for the case when $b = 1$ and sediment transport is entirely local. Values of $b < 1$ imply that particles travel relatively long distances in one direction. We can incorporate nonlocality into the theory for topographic roughness by relying on rules for derivatives in wavenumber domain,

$$\hat{\zeta}(k, t) = \hat{\zeta}(k, 0) e^{[ik]^{b+1} Kt}, \quad (30)$$

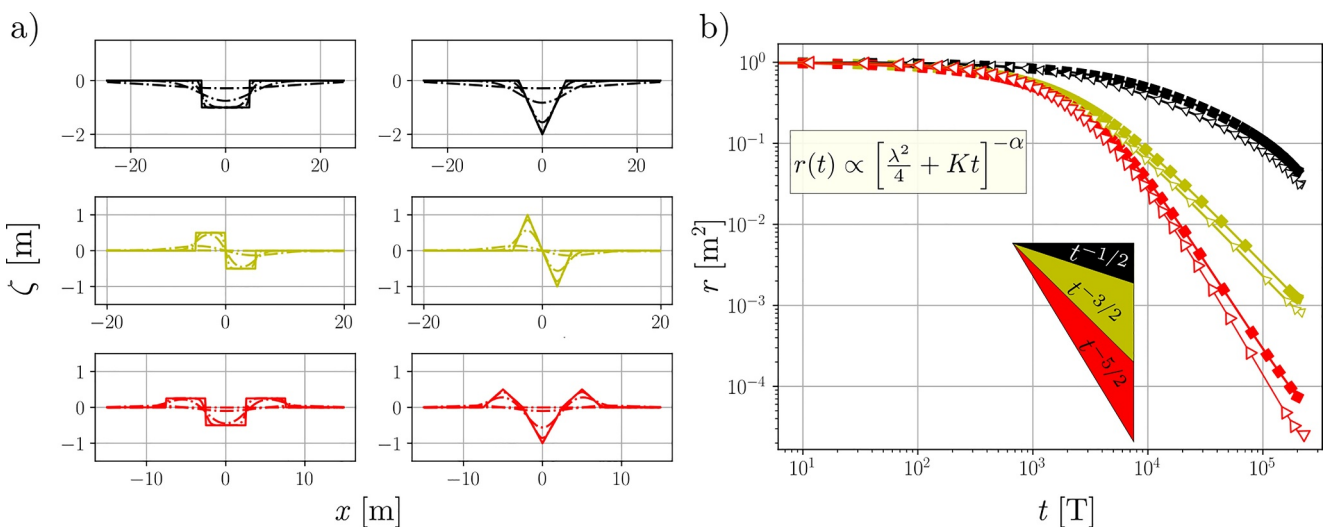


Figure 12. (a) Initial conditions (solid) composed of box and triangular functions that resemble pits, pit-mound couplets, and mound-pit-mound complexes and their forms as they diffuse (dot-dash). (b) Topographic variance for square (square symbols) and triangular (triangular symbols) initial conditions decays approximately the same as the theory describes for DoG's with alpha equal to 1/2, 3/2, and 5/2 for the three conditions (triangular insert).

where K is still a topographic diffusivity but has units [$L^{b+1} T^{-1}$]. There is no analytical solution for Parseval's theorem when $b < 1$, so we must numerically integrate the square of (Equation 30). Figures 11b and 11c illustrate that adding nonlocality increases the pace of topographic smoothing. For example, for the case where $n = 2$ (2nd order DoG, mound-pit-mound), a local formulation results in topographic variance that decays as $t^{-5/2}$ whereas for the nonlocal case with $b = 1/2$, the topographic variance decays as approximately t^{-3} . To be clear, when implementing a nonlocal model for sediment transport, one needs to be careful with the boundary conditions and the direction of the operation. We have applied the operation in one direction for illustration. This simple analysis illustrates the effect of nonlocality on the decay of topographic roughness.

4.3. Generalizing Noisy Roughening Processes

Until this point, we have assumed that roughening processes (shrub mound death, tree throw, avulsions, impact cratering in terms of number per unit area per unit time) are white noises through time. This may not be true for shrub mounds which respond to population dynamics (Gearon & Young, 2020; Worman & Furbish, 2019) and alluvial fans which may repulse or attract new channels (Hajek & Wolinsky, 2012; Martin & Edmonds, 2022). We anticipate that correlation in the time-series will affect the statistics of measured roughness values. In this section, we generalize an expression for the decay of topographic variance and use it to define a characteristic timescale. Then, we develop a numerical technique for generating noisy signals with a specified correlation (AR(1) process) and probability distribution.

To begin, we define a characteristic timescale for the decay of topographic variance using the generalized decay function (Equation 28),

$$\tau_K(\alpha) = \int_0^\infty \frac{r(t)}{r(0)} dt = \left[\frac{\lambda^2}{4} \right]^\alpha \int_0^\infty \left[\frac{\lambda^2}{4} + Kt \right]^{-\alpha} dt = \frac{\lambda^2}{4K[\alpha-1]} \quad \text{for } \alpha > 1 \quad (31)$$

For $\alpha \leq 1$, the upper limit of integration would be set to T_0 , the saturation timescale from Sections 3.3 or 3.1. A comparison between τ_K and the correlation timescale for p , $(\tau_p)[t]$, will reveal how the noise-producing process can lead to different statistics of topographic roughness. The AR(1) process that represents $p(t)$ is

$$p(i+1) = \phi_1 p(i) + \eta, \quad (32)$$

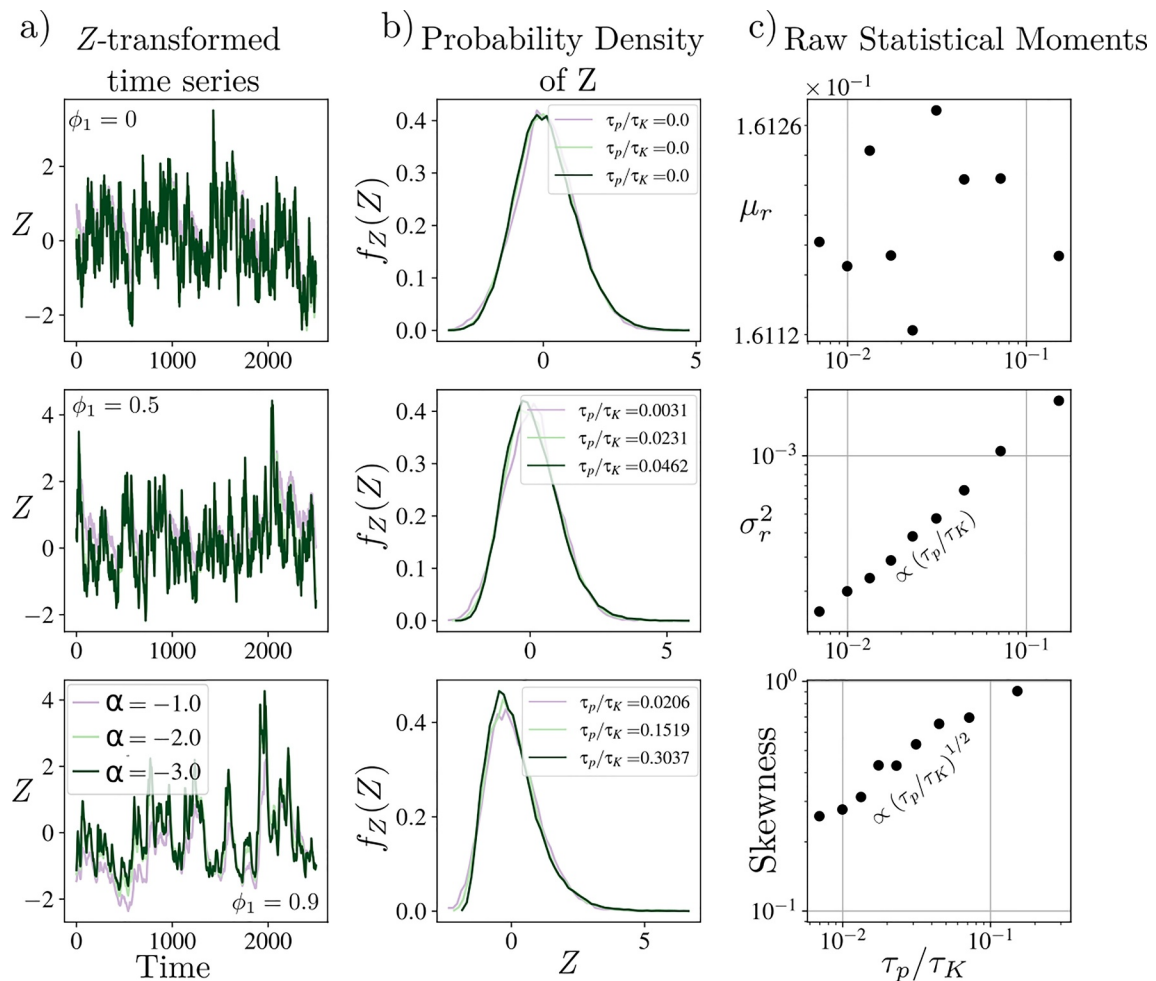


Figure 13. (a) Z-transformed time-series for different combinations of ϕ_1 and α . (b) Probability distributions of Z-transformed roughness values illustrating that the skewness changes as the ratio τ_p/τ_K changes. (c) The raw statistical moments as a function of τ_p/τ_K . The mean is not a function of τ_p/τ_K , the variance of roughness is linearly related to τ_p/τ_K and the skewness of roughness varies as the square root of τ_p/τ_K . That skewness and variance scale with the correlation structure of the roughening process is potentially useful for unfolding the temporal dynamics of shrub populations, tree throw, or avulsions.

where i is a discrete moment in time and η is a random value drawn from a zero-mean Normal distribution. When $\phi_1 = 0$, the signal is a white noise and when $\phi_1 = 1$, the signal is Brownian. The correlation timescale for noisy signals is determined by integrating the autocorrelation function. For AR(1) processes, the correlation timescale is

$$\tau_p = -\frac{1}{\log(\phi_1)}. \quad (33)$$

We then convolve different decay rates according to Equation 28 with different noisy signals to investigate how the characteristics of time series of the roughening processes influence topographic roughness across a landscape. The key value is the ratio of timescales for roughness production versus roughness removal, τ_p/τ_K . However, in addition to specifying the correlation timescale of $p(t)$, we also want to specify the probability distribution that it is drawn from. To do so, we develop a sampling method that resembles the QPPQ method that is popular in studies of stream discharge (Worland et al., 2019).

Using this sampling method we are able to explore the role of correlation in the time series of the roughening process and its influence on the statistics of measured topographic roughness. We numerically simulate the convolution

$$g(t) = C_0 \int_{-\infty}^t p(t') \left[\frac{\lambda^2}{4} + K[t - t'] \right]^{-\alpha} dt', \quad (34)$$

where C_0 is a constant that would normally reflect the geometry of features. To illustrate the effect of different correlation in roughening processes on topographic roughness itself, we set C_0 equal to one. The numerical experiment varies ϕ_1 (0–1) and α (1–3) so that we can explore the effect of τ_p/τ_K . In each run, p is distributed exponentially. Each time series g is Z-transformed so that $Z = (g - \mu_g)/\sigma_g$ which plots all time-series around the same values. Figure 13a illustrates that for a single value of ϕ_p but different values of α , the time-series of Z remains largely the same. Differences between Z time series begin to appear when there is strong correlation in p . The probability distributions of Z-transformed time series highlight the increasing skewness as τ_p/τ_K increases. Figure 13c calculates the statistical moments for $g(t)$, for different values of ϕ_1 in p , but only for $\alpha = 2$ (geometry for tree throw) and illustrates that the mean values remain the same as τ_p/τ_K changes, the variance increases linearly with τ_p/τ_K , and the skewness increases as $(\tau_p/\tau_K)^{1/2}$. These results are likely influenced by our demand that p be distributed as an exponential; however, the fact that the skewness and variance of a distribution reflect the correlation in the time-series is a potentially useful relationship for using the static signal of topographic roughness to infer something about the structure of the time series of shrub population dynamics (Worman & Furbish, 2019), wind throw frequency (Doane et al., 2023), avulsion clustering (Brooke et al., 2022), or impact rates.

5. Conclusions

We have presented a theory that explains topographic roughness in a variety of settings where specified ecologic, atmospheric, and hydrogeomorphic events stochastically add topographic roughness to the land surface. The theory is built on simple assumptions that sediment on soil- and sediment-mantled systems moves faster downhill on steeper slopes and roughness is randomly produced by geomorphic processes that leave a characteristic topographic signature. The theory explains that topographic roughness, quantified by the variance over a specified area, emerges as a simple balance of the frequency of processes that create roughness and the magnitude of the smaller scale processes that remove it. The geometric forms for roughness elements can be one of three classes: mounds (pits), pit-mound couplets, or mound-pit-mound complexes, which are represented by the zero, first, and second order derivatives of Gaussian functions (DoGs) respectively. Specific examples include mounds under shrubs, tree throw pit-mound couplets, channel-levee complexes, and cratered terrain. We demonstrate and develop expressions for the relationship between measured topographic roughness, production rate, and the magnitude of creep-like processes that remove roughness. We demonstrate that topographic roughness scales linearly with the frequency of production process and inversely with the magnitude of creep-like processes. We emphasize that insofar as each of these processes is challenging to observe on human timescales, topographic roughness serves as a valuable archive of stochastic geomorphic processes and extreme events.

In addition to the idealized forms represented by integer order DoGs, we demonstrate that the theory holds for a continuum of initial conditions and is applicable to a broad range of natural features. Theory also applies to topographic features that are better described by triangular or square waves, which illustrates that topographic variance is a robust metric that can be used to quantify a broad range of processes. This is largely because diffusion problems approach a consistent form that is a DoG.

We also consider the consequences of changing correlation timescales of the noisy processes that create topographic roughness. This may include events such as prolonged drought killing many shrubs (Worman & Furbish, 2019), canopy gaps increasing the frequency of wind throw, or avulsions that are clumped in space in time (Brooke et al., 2022). Adding correlation in the time-series appears to add skewness to probability distributions of measured roughness values.

Altimetric data has become finer in resolution and more widely available in the last decade, a trend likely to continue. We demonstrated how static snapshots of high-resolution topographic data can be inverted to obtain process-level details stretching back in time. Our approach makes use of all detailed topographic information rather than coarse scale versions of topography. We aim to provide theory that allows us to augment a coarse-scale and process agnostic perspective of the land surface with a process-specific one. There is, admittedly, much work

to be done to realize topographic roughness as a reliable archive of specific processes; however, the theory presented here indicates that it is possible and demonstrates the type of information that is potentially encoded in the details of topography.

List of Variables

A_n	Amplitude [L^{n+1}]
α	Exponent on the decay rate for topographic roughness [-]
b	Locality of derivative for sediment transport [-]
C	Placeholder coefficient that changes units [varies]
D_n	Dimensionality of the feature (one or two) [-]
H	Domain area or length [L or L^2]
k	Wavenumber [L^{-1}]
λ	Length scale of roughness element [L]
T_0	Diffusive timescale [T]
Φ_d	Portion of live shrubs that die in a year [-]
Φ_{pm}	Aspect ratio of pit-mound couplets [-]
Φ_c	Ratio of amplitudes of zero to second-order DoG that are summed together [-]
Φ_1	R(1) parameter
K	Topographic Diffusivity [$L^2 T^{-1}$]
n	Order of DoG
η	Noise in AR(1) process [-]
p	Roughness Production Rate [T^{-1}]
r	Topographic Roughness [L^2]
r_s	Topographic Roughness due to a single element (pit, pit-mound couplet, etc.) [L^2]
R	Radius of crater [L]
S_a	Number of live shrubs [#]
μ_m	Expected value of variable m [units of m]
σ_m^2	Variance of variable m [units of m^2]
t	Time [T]
τ_K	Characteristic timescale of diffusion [T]
τ_p	Correlation timescale of roughening process [T]
x	Horizontal distance [L]
ζ	Land surface elevation [L]
$\hat{\zeta}$	Fourier transform of land surface elevation [L^2]
ζ_s	Topography of a single element (pit, pit-mound couplet, mound-pit-mound complex) [L^2]

Conflict of Interest

The authors declare no conflicts of interest relevant to this study.

Data Availability Statement

Data and codes for this article are available in Doane (2024).

Acknowledgments

The authors thank Will Struble and an anonymous reviewer for thoughtful reviews that helped to strengthen this paper. THD, BYJ, and DAE acknowledge funding by NSF-EAR 2218293. DAE and JHG also acknowledge funding by NSF-EAR 2321056.

References

- Adams, P. N., Slingerland, R. L., & Smith, N. D. (2004). Variations in natural levee morphology in anastomosed channel flood plain complexes. *Geomorphology*, 61(1–2), 127–142. <https://doi.org/10.1016/j.geomorph.2003.10.005>
- Berendsen, H. J. A., & Stouthamer, E. (2002). Paleogeographic evolution and avulsion history of the Holocene Rhine-Meuse delta, The Netherlands. *Netherlands Journal of Geosciences - Geologie En Mijnbouw*, 81(1), 97–112. <https://doi.org/10.1017/s0016774600020606>
- Bochet, E., Poesen, J., & Rubio, J. L. (2000). Mound development as an interaction of individual plants with soil, water erosion and sedimentation processes on slopes. *Earth Surface Processes and Landforms*, 25(8), 847–867. [https://doi.org/10.1002/1096-9837\(200008\)25:8<847::aid-esp103>3.0.co;2-q](https://doi.org/10.1002/1096-9837(200008)25:8<847::aid-esp103>3.0.co;2-q)
- Booth, A. M., LaHusen, S. R., Duvall, A. R., & Montgomery, D. R. (2017). Holocene history of deep-seated landsliding in the North Fork Stillaguamish River valley from surface roughness analysis, radiocarbon dating, and numerical landscape evolution modeling. *Journal of Geophysical Research: Earth Surface*, 122(2), 456–472. <https://doi.org/10.1002/2016jf003934>
- Brooke, S., Chadwick, A. J., Silverstre, J., Lamb, M. P., Edmonds, D. A., & Ganti, V. (2022). Where rivers jump course. *Science*, 376, 897–990. <https://doi.org/10.1126/science.abm1215>
- Buis, E., Temme, A. J. A. M., Veldkamp, A., Boeken, B., Jongmans, A. G., van Breemen, N., & Schoorl, J. M. (2010). Shrub mound formation and stability on semi-arid slopes in the northern Negev desert of Israel: A field and simulation study. *Geoderma*, 156(3–4), 363–371. <https://doi.org/10.1016/j.geoderma.2010.03.005>
- Cai, Y., & Fa, W. (2020). Meter-scale topographic roughness of the Moon: The effect of small impact craters. *Journal of Geophysical Research: Planets*, 125(8). <https://doi.org/10.1029/2020je006429>
- Campbell, B. A., Putzig, N. E., Carter, L. M., Morgan, G. A., Phillips, R. J., & Plaut, J. J. (2013). Roughness and near-surface density of Mars from SHARAD radar echoes. *Journal of Geophysical Research: Planets*, 118(3), 436–450. <https://doi.org/10.1002/jgre.20050>
- Cannon, J. B., Peterson, C. J., O'Brien, J. J., & Brewer, J. S. (2017). A review and classification of interactions between forest disturbance from wind and fire. *Forest Ecology and Management*, 406, 381–390. <https://doi.org/10.1016/j.foreco.2017.07.035>
- Cao, W., Xiao, Z., Luo, F., Ma, Y., & Xu, R. (2023). Comparison of topographic roughness of layered deposits on Mars. *Remote Sensing*, 15(9), 2272. <https://doi.org/10.3390/rs15092272>
- Clubb, F. J., Mudd, S. M., Attal, M., Milodowski, D. T., & Grieve, S. W. D. (2016). The relationship between drainage density, erosion rate, and hilltop curvature: Implications for sediment transport processes. *Journal of Geophysical Research: Earth Surface*, 121(10), 1724–1745. <https://doi.org/10.1002/2015jf003747>
- Culling, W. E. H. (1963). Soil creep and the development of hillside slopes. *The Journal of Geology*, 71(2), 127–161. <https://doi.org/10.1086/626891>
- DeLisle, C., & Yanites, B. J. (2023). Rethinking variability in bedrock rivers: Sensitivity of hillslope sediment supply to precipitation events modulates bedrock incision during floods. *Journal of Geophysical Research: Earth Surface*, 128(9). <https://doi.org/10.1029/2023jf007148>
- Del Vecchio, J., DiBiase, R. A., Denn, A. R., Bierman, P. R., Caffee, M. W., & Zimmerman, S. R. (2018). Record of coupled hillslope and channel response to Pleistocene erosion and deposition in a sandstone headwater valley, central Pennsylvania. *GSA Bulletin*, 130(11–12), 1903–1917. <https://doi.org/10.1130/b31912.1>
- DiBiase, R. A., Lamb, M. P., Ganti, V., & Booth, A. M. (2017). Slope, grain size, and roughness controls on dry sediment transport and storage on steep hillslopes. *Journal of Geophysical Research: Earth Surface*, 122(4), 941–960. <https://doi.org/10.1002/2016jf003970>
- Doane, T. H. (2024). tdoane/TopographicRoughness: Python files for Doane et al. (2024) [Software]. Zenodo. <https://doi.org/10.5281/zenodo.13226632>
- Doane, T. H., Edmonds, D., Yanites, B. J., & Lewis, Q. (2021). Topographic roughness on forested hillslopes: A theoretical approach for quantifying hillslope sediment flux from tree throw. *Geophysical Research Letters*, 48(20). <https://doi.org/10.1029/2021gl094987>
- Doane, T. H., Yanites, B. J., Edmonds, D. A., & Novick, K. A. (2023). Hillslope roughness reveals forest sensitivity to extreme winds. *Proceedings of the National Academy of Sciences*, 120(3). <https://doi.org/10.1073/pnas.2212105120>
- Du, H. D., Jiao, J. Y., Jia, Y. F., Wang, N., & Wang, D. L. (2013). Phylogenetic mounds of four typical shoot architecture species at different slope gradients on the Loess Plateau of China. *Geomorphology*, 193, 57–64. <https://doi.org/10.1016/j.geomorph.2013.04.002>
- Edmonds, D. A., Hajek, E. A., Downton, N., & Bryk, A. B. (2016). Avulsion flow-path selection on rivers in foreland basins. *Geology*, 44(9), 695–698. <https://doi.org/10.1130/g38082.1>
- Fassett, C. I. (2016). Analysis of impact crater populations and the geochronology of planetary surfaces in the inner solar system. *Journal of Geophysical Research: Planets*, 121(10), 1900–1926. <https://doi.org/10.1002/2016JE005094>
- Fassett, C. I., & Thomson, B. J. (2014). Crater degradation on the lunar maria: Topographic diffusion and the rate of erosion on the Moon. *Journal of Geophysical Research: Planets*, 119(10), 2255–2271. <https://doi.org/10.1002/2014je004698>
- Fernandes, N. F., & Dietrich, W. E. (1997). Hillslope evolution by diffusive processes: The timescale for equilibrium adjustments. *Water Resources Research*, 33(6), 1307–1318. <https://doi.org/10.1029/97wr00534>
- Finnegan, N. J., Perkins, J. P., Nereson, A. L., & Handwerger, A. L. (2021). Unsaturated flow processes and the onset of seasonal deformation in slow-moving landslides. *Journal of Geophysical Research: Earth Surface*, 126(5). <https://doi.org/10.1029/2020JF005758>
- Foufoula-Georgiou, E., Ganti, V., & Dietrich, W. E. (2010). A nonlocal theory of sediment transport on hillslopes. *Journal of Geophysical Research*, 115(F2). <https://doi.org/10.1029/2009jf001280>
- Frankel, K. L., & Dolan, J. F. (2007). Characterizing arid region alluvial fan surface roughness with airborne laser swath mapping digital topographic data. *Journal of Geophysical Research*, 112(F2). <https://doi.org/10.1029/2006jf000644>
- Furbish, D. J., Childs, E. M., Haff, P. K., & Schmeeckle, M. W. (2009). Rain splash of soil grains as a stochastic advection-dispersion process, with implications for desert plant-soil interactions and land-surface evolution. *Journal of Geophysical Research*, 114(F3). <https://doi.org/10.1029/2009jf001265>
- Furbish, D. J., & Fagherazzi, S. (2001). Stability of creeping soil and implications for hillslope evolution. *Water Resources Research*, 37(10), 2607–2618. <https://doi.org/10.1029/2001wr000239>
- Furbish, D. J., & Haff, P. K. (2010). From divots to swales: Hillslope sediment transport across divers length scales. *Journal of Geophysical Research*, 115(F3). <https://doi.org/10.1029/2009jf001576>

- Furbish, D. J., & Roering, J. J. (2013). Sediment disentrainment and the concept of local versus nonlocal transport on hillslopes. *Journal of Geophysical Research: Earth Surface*, 118(2), 937–952. <https://doi.org/10.1002/jgrf.20071>
- Furbish, D. J., Roering, J. J., Doane, T. H., Roth, D. L., Williams, S. G. W., & Abbott, A. M. (2021). Rarefied particle motions on hillslopes – Part 1: Theory. *Earth Surface Dynamics*, 9(3), 539–576. <https://doi.org/10.5194/esurf-9-539-2021>
- Gabet, E. J., & Mendoza, M. K. (2012). Particle transport over rough hillslope surfaces by dry ravel: Experiments and simulations with implications for nonlocal sediment flux. *Journal of Geophysical Research*, 117(F1). <https://doi.org/10.1029/2011jf002229>
- Gabet, E. J., & Mudd, S. M. (2010). Bedrock erosion by root fracture and tree throw: A coupled biogeomorphic model to explore the humped soil production function and the persistence of hillslope soils. *Journal of Geophysical Research*, 115(F4). <https://doi.org/10.1029/2009jf001526>
- Gabet, E. J., Mudd, S. M., Wood, R. W., Grieve, S. W. D., Binnie, S. A., & Dunai, T. J. (2021). Hilltop curvature increases with the square root of erosion rate. *Journal of Geophysical Research: Earth Surface*, 126(5). <https://doi.org/10.1029/2020jf005858>
- Gabet, E. J., Reichman, O. J., & Seabloom, E. W. (2003). The effects of bioturbation on soil processes and sediment transport. *Annual Review of Earth and Planetary Sciences*, 31(1), 249–273. <https://doi.org/10.1146/annurev.earth.31.100901.141314>
- Ganti, V., Passalacqua, P., & Foufoula-Georgiou, E. (2012). A sub-grid scale closure for nonlinear hillslope sediment transport models. *Journal of Geophysical Research*, 117(F2). <https://doi.org/10.1029/2011jf002181>
- Gardiner, B., Berry, P., & Moulia, B. (2016). Review: Wind impacts on plant growth, mechanics and damage. *Plant Science*, 245, 94–118. <https://doi.org/10.1016/j.plantsci.2016.01.006>
- Gault, D. E. (1970). Saturation and equilibrium conditions for impact cratering on the lunar surface: Criteria and implications. *Radio Science*, 5(2), 273–291. <https://doi.org/10.1029/rs005i002p00273>
- Gearon, J., Martin, H., DeLisle, C., Barefoot, E., Mohrig, D., Paola, C., & Edmonds, D. (2024). Rules of river avulsion change downstream. *Nature*. <https://doi.org/10.21203/rs.3.rs-3660956/v1>
- Gearon, J. H., & Young, M. H. (2020). Geomorphic controls on shrub canopy volume and spacing of creosote bush in northern Mojave Desert, USA. *Landscape Ecology*, 36(2), 527–547. <https://doi.org/10.1007/s10980-020-01149-8>
- Godfrey, C. M., & Peterson, C. J. (2017). Estimating enhanced Fujita scale levels based on forest damage severity. *Weather and Forecasting*, 32(1), 243–252. <https://doi.org/10.1175/waf-d-16-0104.1>
- Grieve, S. W. D., Mudd, S. M., Milodowski, D. T., Clubb, F. J., & Furbish, D. J. (2016). How does grid-resolution modulate the topographic expression of geomorphic processes? *Earth Surface Dynamics*, 4(3), 627–653. <https://doi.org/10.5194/esurf-4-627-2016>
- Guo, D., Fa, W., Wu, B., Li, Y., & Liu, Y. (2021). Millimeter- to decimeter-scale surface roughness of the Moon at the Chang'e-4 exploration region. *Geophysical Research Letters*, 48(19). <https://doi.org/10.1029/2021gl094931>
- Hajek, E. A., & Edmonds, D. A. (2014). Is river avulsion style controlled by floodplain morphodynamics? *Geology*, 42(3), 199–202. <https://doi.org/10.1130/g35045.1>
- Hajek, E. A., & Wolinsky, M. A. (2012). Simplified process modeling of river avulsion and alluvial architecture: Connecting models and field data. *Sedimentary Geology*, 257–260, 1–30. <https://doi.org/10.1016/j.sedgeo.2011.09.005>
- Hancock, G., & Lowry, J. (2021). Quantifying the influence of rainfall, vegetation and animals on soil erosion and hillslope connectivity in the monsoonal tropics of northern Australia. *Earth Surface Processes and Landforms*, 46(10), 2110–2123. <https://doi.org/10.1002/esp.5147>
- Hassan, M. A., & Reid, I. (1990). The influence of microform bed roughness elements on flow and sediment transport in gravel bed rivers. *Earth Surface Processes and Landforms*, 15(8), 739–750. <https://doi.org/10.1002/esp.3290150807>
- Hellmer, M. C., Rios, B. A., Ouimet, W. B., & Sibley, T. R. (2015). Ice storms, tree throw, and hillslope sediment transport in northern hardwood forests. *Earth Surface Processes and Landforms*, 40(7), 901–912. <https://doi.org/10.1002/esp.3690>
- Henriksen, M. R., Manheim, M. R., Burns, K. N., Seymour, P., Speyerer, E. J., Deran, A., et al. (2017). Extracting accurate and precise topography from LROC narrow angle camera stereo observations. *Icarus*, 283, 122–137. <https://doi.org/10.1016/j.icarus.2016.05.012>
- Johnstone, S. A., Hudson, A. M., Nicovich, S., Ruleman, C. A., Sare, R. M., & Thompson, R. A. (2018). Establishing chronologies for alluvial-fan sequences with analysis of high-resolution topographic data: San Luis Valley, Colorado, USA. *Geosphere*, 14(6), 2487–2504. <https://doi.org/10.1130/ges01680.1>
- Jyotsna, R., & Haff, P. K. (1997). Microtopography as an indicator of modern hillslope diffusivity in arid terrain. *Geology*, 25(8), 695. [https://doi.org/10.1130/0091-7613\(1997\)025<0695:maaiom>2.3.co;2](https://doi.org/10.1130/0091-7613(1997)025<0695:maaiom>2.3.co;2)
- Kean, J. W., & Smith, J. D. (2006). Form drag in rivers due to small-scale natural topographic features: 1. Regular sequences. *Journal of Geophysical Research*, 111(F4). <https://doi.org/10.1029/2006jf000467>
- Kreslavsky, M. A., Head, J. W., Neumann, G. A., Rosenburg, M. A., Aharonson, O., Smith, D. E., & Zuber, M. T. (2013). Lunar topographic roughness maps from Lunar Orbiter Laser Altimeter (LOLA) data: Scale dependence and correlation with geologic features and units. *Icarus*, 226(1), 52–66. <https://doi.org/10.1016/j.icarus.2013.04.027>
- Kreslavsky, M. A., Head, J. W., Neumann, G. A., Zuber, M. T., & Smith, D. E. (2014). Kilometer-scale topographic roughness of Mercury: Correlation with geologic features and units. *Geophysical Research Letters*, 41(23), 8245–8251. <https://doi.org/10.1002/2014GL062162>
- Kumar, P., & Foufoula-Georgiou, E. (1997). Wavelet analysis for geophysical applications. *Reviews of Geophysics*, 35(4), 385–412. <https://doi.org/10.1029/97rg00427>
- LaHusen, S. R., Duvall, A. R., Booth, A. M., & Montgomery, D. R. (2016). Surface roughness dating of long-runout landslides near Oso, Washington (USA), reveals persistent postglacial hillslope instability. *Geology*, 44(2), 111–114. <https://doi.org/10.1130/g37267.1>
- Lashermes, B., Foufoula-Georgiou, E., & Dietrich, W. E. (2007). Channel network extraction from high resolution topography using wavelets. *Geophysical Research Letters*, 34(23). <https://doi.org/10.1029/2007gl031140>
- Lewis, Q. W., Edmonds, D. A., & Yanites, B. J. (2020). Integrated UAS and LiDAR reveals the importance of land cover and flood magnitude on the formation of incipient chute holes and chute cutoff development. *Earth Surface Processes and Landforms*, 45(6), 1441–1455. <https://doi.org/10.1002/esp.4816>
- Lindroth, A., Lagergren, F., Grelle, A., Klemedtsson, L., Langvall, O., Weslien, P., & Tuulik, J. (2009). Storms can cause Europe-wide reduction in forest carbon sink. *Global Change Biology*, 15(2), 346–355. <https://doi.org/10.1111/j.1365-2486.2008.01719.x>
- Luetzenburg, G., Kroon, A., & Björk, A. A. (2021). Evaluation of the Apple iPhone 12 Pro LiDAR for an application in geosciences. *Scientific Reports*, 11(1), 22221. <https://doi.org/10.1038/s41598-021-01763-9>
- Madoff, R. D., & Putkonen, J. (2016). Climate and hillslope degradation vary in concert: 85 ka to present, eastern Sierra Nevada, CA, USA. *Geomorphology*, 266, 33–40. <https://doi.org/10.1016/j.geomorph.2016.05.010>
- Madoff, R. D., & Putkonen, J. (2022). Global variations in regional degradation rates since the Last Glacial Maximum mapped through time and space. *Quaternary Research*, 109, 128–140. <https://doi.org/10.1017/qua.2022.4>
- Martin, H. K., & Edmonds, D. A. (2022). The push and pull of abandoned channels: How floodplain processes and healing affect avulsion dynamics and alluvial landscape evolution in foreland basins. *Earth Surface Dynamics*, 10, 555–579. <https://doi.org/10.5194/esurf-10-555-2022>

- Martin, H. K., & Edmonds, D. A. (2023). Avulsion dynamics determine fluvial fan morphology in a cellular model. *Geology*, 51(8), 796–800. <https://doi.org/10.1130/g51138.1>
- Melosh, H. J. (1989). *Impact cratering: A geologic process*. Oxford University Press.
- Milodowski, D. T., Mudd, S. M., & Mitchard, E. T. A. (2015). Topographic roughness as a signature of the emergence of bedrock in eroding landscapes. *Earth Surface Dynamics*, 3(4), 483–499. <https://doi.org/10.5194/esurf-3-483-2015>
- Mohrig, D., Heller, P. L., Paola, C., & Lyons, W. J. (2000). *Geological Society of America Bulletin*, 112(12), 1787. [https://doi.org/10.1130/0016-7606\(2000\)112<1787:iapfaa>2.0.co;2](https://doi.org/10.1130/0016-7606(2000)112<1787:iapfaa>2.0.co;2)
- Nikora, V., McLean, S., Coleman, S., Pokrajac, D., McEwan, I., Campbell, L., et al. (2007). Double-averaging concept for rough-bed open-channel and overland flows: Applications. *Journal of Hydraulic Engineering*, 133(8), 884–895. [https://doi.org/10.1061/\(asce\)0733-9429\(2007\)133:8\(884\)](https://doi.org/10.1061/(asce)0733-9429(2007)133:8(884))
- Norman, S. A., Schaetzl, R. J., & Small, T. W. (1995). Effects of slope angle on mass movement by tree uprooting. *Geomorphology*, 14(1), 19–27. [https://doi.org/10.1016/0169-555X\(95\)00016-x](https://doi.org/10.1016/0169-555X(95)00016-x)
- Orosei, R., Bianchi, R., Coradini, A., Espinasse, S., Federico, C., Ferriccioli, A., & Gavishin, A. I. (2003). Self-affine behavior of Martian topography at kilometer scale from Mars Orbiter Laser Altimeter data. *Journal of Geophysical Research*, 108(E4). <https://doi.org/10.1029/2002je001883>
- Parsons, A. J., Abrahams, A. D., & Simanton, J. R. (1992). Microtopography and soil-surface materials on semi-arid piedmont hillslopes, southern Arizona. *Journal of Arid Environments*, 22(2), 107–115. [https://doi.org/10.1016/s0140-1963\(18\)30585-8](https://doi.org/10.1016/s0140-1963(18)30585-8)
- Pelletier, J. D., & Turcotte, D. L. (1997). Synthetic stratigraphy with a stochastic diffusion model of fluvial sedimentation. *Journal of Sedimentary Research*, 67(6), 1060–1067. <https://doi.org/10.1306/D42686C6-2B26-11D7-8648000102C1865D>
- Phillips, J. D., Šamonil, P., Pawlik, Ł., Trochta, J., & Daněk, P. (2017). Domination of hillslope denudation by tree uprooting in an old-growth forest. *Geomorphology*, 276, 27–36. <https://doi.org/10.1016/j.geomorph.2016.10.006>
- Reitz, M. D., & Jerolmack, D. J. (2012). Experimental alluvial fan evolution: Channel dynamics, slope controls, and shoreline growth. *Journal of Geophysical Research*, 117(F2). <https://doi.org/10.1029/2011jf002261>
- Richardson, P., & Karlstrom, L. (2019). The multi-scale influence of topography on lava flow morphology. *Bulletin of Volcanology*, 81(4), 21. <https://doi.org/10.1007/s00445-019-1278-9>
- Richardson, P. W., Perron, J. T., & Schurr, N. D. (2019). Influences of climate and life on hillslope sediment transport. *Geology*, 47(5), 423–426. <https://doi.org/10.1130/g45305.1>
- Ricketts, J. W., Kelley, S. A., Karlstrom, K. E., Schmandt, B., Donahue, M. S., & van Wijk, J. (2016). Synchronous opening of the Rio Grande rift along its entire length at 25–10 Ma supported by apatite (U-Th)/He and fission-track thermochronology, and evaluation of possible driving mechanisms. *Geological Society of America Bulletin*, 128(3–4), 397–424. <https://doi.org/10.1130/b31223.1>
- Roering, J. J., Kirchner, J. W., & Dietrich, W. E. (1999). Evidence for nonlinear, diffusive sediment transport on hillslopes and implications for landscape morphology. *Water Resources Research*, 35(3), 853–870. <https://doi.org/10.1029/1998wr900090>
- Roering, J. J., Mackey, B. H., Handwerger, A. L., Booth, A. M., Schmidt, D. A., Bennett, G. L., & Cerovski-Darria, C. (2015). Beyond the angle of repose: A review and synthesis of landslide processes in response to rapid uplift, Eel river, northern California. *Geomorphology*, 236, 109–131. <https://doi.org/10.1016/j.geomorph.2015.02.013>
- Roering, J. J., Marshall, J., Booth, A. M., Mort, M., & Jin, Q. (2010). Evidence for biotic controls on topography and soil production. *Earth and Planetary Science Letters*, 298(1–2), 183–190. <https://doi.org/10.1016/j.epsl.2010.07.040>
- Roering, J. J., Perron, J. T., & Kirchner, J. W. (2007). Functional relationships between denudation and hillslope form and relief. *Earth and Planetary Science Letters*, 264(1–2), 245–258. <https://doi.org/10.1016/j.epsl.2007.09.035>
- Roth, D. L., Doane, T. H., Roering, J. J., Furbish, D. J., & Zettler-Mann, A. (2020). Particle motion on burned and vegetated hillslopes. *Proceedings of the National Academy of Sciences*, 117(41), 25353–25343. <https://doi.org/10.1073/pnas.1922495117>
- Šamonil, P., Egli, M., Steinert, T., Norton, K., Abiven, S., Daněk, P., et al. (2019). Soil denudation rates in an old-growth mountain temperate forest driven by tree uprooting dynamics, Central Europe. *Land Degradation & Development*, 31(2), 222–239. <https://doi.org/10.1002/lrd.3443>
- Schumer, R., Meerschaert, M. M., & Baeumer, B. (2009). Fractional advection-dispersion equations for modeling transport at the Earth surface. *Journal of Geophysical Research*, 114(F4). <https://doi.org/10.1029/2008jf001246>
- Schumer, R., Taloni, A., & Furbish, D. J. (2017). Theory connecting nonlocal sediment transport, earth surface roughness, and the Sadler effect. *Geophysical Research Letters*, 44(5), 2281–2289. <https://doi.org/10.1029/2016GL072134>
- Seabold, S., & Perktold, J. (2010). Statsmodels: Econometric and statistical modeling with python. In *Proceedings of the 9th Python in Science Conference*.
- Shachak, M., & Lovett, G. M. (1998). Atmospheric deposition to a desert ecosystem and its implications for management. *Ecological Applications*, 8(2), 455–463. [https://doi.org/10.1890/1051-0761\(1998\)008\[0455:adtade\]2.0.co;2](https://doi.org/10.1890/1051-0761(1998)008[0455:adtade]2.0.co;2)
- Slingerland, R., & Smith, N. D. (2004). River avulsions and their deposits. *Annual Review of Earth and Planetary Sciences*, 32(1), 257–285. <https://doi.org/10.1146/annurev.earth.32.101802.120201>
- Smith, M. W. (2014). Roughness in the Earth sciences. *Earth-Science Reviews*, 136, 202–225. <https://doi.org/10.1016/j.earscirev.2014.05.016>
- Soulard, C. E., Esque, T. C., Bedford, D. R., & Bond, S. (2012). The role of fire on soil mounds and surface roughness in the Mojave Desert. *Earth Surface Processes and Landforms*, 38(2), 111–121. <https://doi.org/10.1002/esp.3264>
- Stoker, J., & Miller, B. (2022). The accuracy and consistency of 3D elevation program data: A systematic analysis. *Remote Sensing*, 14(4), 940. <https://doi.org/10.3390/rs144040940>
- Strubel, W. T., & Roering, J. J. (2021). Hilltop curvature as a proxy for erosion rate: Wavelets enable rapid computation and reveal systematic underestimation. *Earth Surface Dynamics*, 9(5), 1279–1300. <https://doi.org/10.5194/esurf-9-1279-2021>
- Tucker, G. E., & Bradley, D. N. (2010). Trouble with diffusion: Reassessing hillslope erosion laws with a particle-based model. *Journal of Geophysical Research*, 115(F1). <https://doi.org/10.1029/2009jf001264>
- Turowski, J. M., Yager, E. M., Badoux, A., Rickenmann, D., & Molnar, P. (2009). The impact of exceptional events on erosion, bedload transport and channel stability in a step-pool channel. *Earth Surface Processes and Landforms*, 34(12), 1661–1673. <https://doi.org/10.1002/esp.1855>
- Valenza, J. M., Edmonds, D. A., Hwang, T., & Roy, S. (2020). Downstream changes in river avulsion style are related to channel morphology. *Nature Communications*, 11(1), 2116. <https://doi.org/10.1038/s41467-020-15859-9>
- Valter, M., & Schaetzl, R. J. (2017). Pit-mound microrelief in forest soils: Review of implications for water retention and hydrologic modelling. *Forest Ecology and Management*, 393, 40–51. <https://doi.org/10.1016/j.foreco.2017.02.048>
- Viles, H. (2016). Technology and geomorphology: Are improvements in data collection techniques transforming geomorphic science? *Geomorphology*, 270, 121–133. <https://doi.org/10.1016/j.geomorph.2016.07.011>
- Wang, Y. (2015). Generalized seismic wavelets. *Geophysical Journal International*, 203(2), 1172–1178. <https://doi.org/10.1093/gji/ggv346>

- Worland, S. C., Steinschneider, S., Farmer, W., Asquith, W., & Knight, R. (2019). Copula theory as a generalized framework for flow-duration curve based streamflow estimates in ungaged and partially gaged catchments. *Water Resources Research*, 55(11), 9378–9397. <https://doi.org/10.1029/2019wr025138>
- Worman, S. L., & Furbish, D. J. (2019). A probabilistic, biologically informed model of desert shrub population dynamics with the granularity appropriate for geomorphic simulations. *Earth Surface Processes and Landforms*, 44(6), 1221–1232. <https://doi.org/10.1002/esp.4568>
- Xiao, Z., & Werner, S. C. (2015). Size-frequency distribution of crater populations in equilibrium on the Moon. *Journal of Geophysical Research: Planets*, 120(12), 2277–2292. <https://doi.org/10.1002/2015je004860>
- Yager, E. M., Kirchner, J. W., & Dietrich, W. E. (2007). Calculating bed load transport in steep boulder bed channels. *Water Resources Research*, 43(7). <https://doi.org/10.1029/2006wr005432>